J. Fluid Mech. (2025), *vol*. 1003, A14, doi:10.1017/jfm.2024.1089

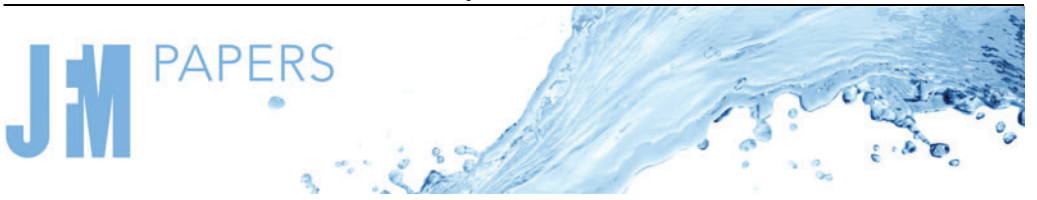

Focussing of concentric free-surface waves

Lohit Kayal[1], **Vatsal Sanjay**[2], **Nikhil Yewale**[1], **Anil Kumar**[1] **and Ratul Dasgupta**[1],†

[1]Department of Chemical Engineering, Indian Institute of Technology, Bombay, 400 076, India

[2]CoMPhy Lab, Physics of Fluids Department, Max Planck Center for Complex Fluid Dynamics, Department of Science and Technology, and J. M. Burgers Centre for Fluid Dynamics, University of Twente, P. O. Box 217, 7500 AE Enschede, The Netherlands

(Received 2 June 2024; revised 1 October 2024; accepted 5 November 2024)

Gravito–capillary waves at free surfaces are ubiquitous in several natural and industrial processes involving quiescent liquid pools bounded by cylindrical walls. These waves emanate from the relaxation of initial interface distortions, which often take the form of a cavity (depression) centred on the symmetry axis of the container. The surface waves reflect from the container walls leading to a radially inward propagating wavetrain converging (focussing) onto the symmetry axis. Under the inviscid approximation and for sufficiently shallow cavities, the relaxation is well-described by the linearised potential-flow equations. Naturally, adding viscosity to such a system introduces viscous dissipation that enervates energy and dampens the oscillations at the symmetry axis. However, for viscous liquids and deeper cavities, these equations are qualitatively inaccurate. In this study, we decompose the initial localised interface distortion into several Bessel functions and study their time evolution governing the propagation of concentric gravito–capillary waves on a free surface. This is carried out for inviscid as well as viscous liquids. For a sufficiently deep cavity, the inward focussing of waves results in large interfacial oscillations at the axis, necessitating a second-order nonlinear theory. We demonstrate that this theory effectively models the interfacial behaviour and highlights the crucial role of nonlinearity near the symmetry axis. This is rationalised via demonstration of the contribution of bound wave components to the interface displacement at the symmetry axis Contrary to expectations, the addition of slight viscosity further intensifies the oscillations at the symmetry axis although the mechanism of wavetrain generation here is quite different compared with bubble bursting where such behaviour is well known (Duchemin *et al.*, *Phys. Fluids*, vol. 14, issue 9, 2002, pp. 3000–3008). This finding underscores the limitations of the potential flow

† Email address for correspondence: dasgupta.ratul@gmail.com

model and suggests avenues for more accurate modelling of such complex free-surface flows.

Key words: capillary waves, surface gravity waves

1. Introduction to wave focussing

Focussing of moderate amplitude, progressive surface waves can often in turn produce unexpectedly large waves. At oceanic scales, spatial wave focussing, where large amplitude waves form persistently in specific regions (Chavarria, Le Gal & Le Bars 2018; Torres *et al.* 2022), can produce waves powerful enough to damage or capsize ships. A famous example is the Aghulas current region (The Editors of Encyclopaedia Britannica 2024) known for giant waves and shipping accidents (Mallory 1974; Smith 1976). The role of current generated refractive focussing leading to the birth of such giant waves, specifically in the Agulhas, was anticipated by Peregrine (1976) (also see figure 8 in Dysthe, Krogstad & Müller (2008) and § 2 in White & Fornberg (1998)). Refractive focussing of surface waves (Peregrine 1986) has also been exploited to design 'lenses', i.e. submerged structures in a water basin which focus incoming divergent, circular waves (see figure 1*a* in Stamnes *et al.* (1983)), these being motivated from wave generation of power (McIver 1985; Murashige & Kinoshita 1992).

In addition to spatial focussing, spatiotemporal focussing also occurs (Dysthe *et al.* 2008), where large wave amplitudes manifest at specific locations in space, albeit briefly. Spatiotemporal focussing has obvious relevance not only towards understanding, for example, rogue (freak) waves in the ocean (Charlie Wood 2020), but also to our current study (next section). The physical mechanisms underlying spatiotemporal focussing have been distinguished further into linear and nonlinear dispersive focussing (§§ 4.2 and 4.3, Dysthe *et al.* (2008)). Linear dispersive focussing of progressive waves relies on constructive interference exploiting the dispersive nature of surface gravity waves and is particularly simple to understand in the deep-water limit. For unidirectional wave packets in deep water, generated from a wavemaker oscillating harmonically at frequency Ω at one end of a sufficiently long wave flume, the energy propagation velocity (group velocity) of the packet is $c_g = g/2\Omega$ where g is acceleration due to gravity. If the wavemaker frequency varies linearly from Ω_1 to Ω_2 ($\Omega_1 > \Omega_2$) following $\mathrm{d}\Omega/\mathrm{d}t = -(g/2x_f)$ within the time interval $[t_1, t_2]$, Longuet-Higgins (1974) showed that the energy of each wave packet emitted during this period will converge at $x = x_f$ simultaneously at $t = t_f$ (see Brown & Jensen 2001). This focussing of wave energy thus causes a momentary but significant increase in energy density at x_f manifested as a transient, large amplitude wave at that location around time t_f. This technique has been discussed in Davis & Zarnick (1964) and its variants have been employed extensively to generate breaking waves in the laboratory in a predictable manner in two (Rapp & Melville 1990) and three dimensions (Johannessen & Swan 2001; Wu & Nepf 2002; McAllister *et al.* 2022) as well as in other related contexts such as generation of a parasitic capillary on large amplitude waves (Xu & Perlin 2023).

On the other hand, in nonlinear dispersive focussing, the modulational instability (Benjamin & Feir 1967) of a uniform, finite-amplitude wavetrain (Stokes wave) plays a crucial role. This instability can cause the wavetrain to split into groups, where focussing within a group can produce a wave significantly larger than the others (Zakharov, Dyachenko & Prokofiev 2006). For further details on nonlinear focussing, we refer readers to the review by Onorato *et al.* (2013).

1.1. *Spatiotemporal focussing at gravito–capillary scales*

Following this brief introduction to large-scale focussing, we now shift our attention to length scales where gravitational and capillary restoring forces are nearly equivalent. Our study aims to achieve an analytical understanding of wave focussing at these shorter scales. Below, we illustrate two examples where such small-scale focussing can be readily observed.

Stuhlman (1932) investigated the formation of drops from collapsing bubbles with diameters under 0.12 cm in water–air interfaces and 0.15 cm in benzene–air interfaces. He hypothesised that these drops emerged from Worthington jets created by the collapse of the bubble cavity. However, contemporary research identifies this as just one of two mechanisms responsible for drop generation (Villermaux, Wang & Deike 2022). The first high-speed (≈6000 frames per second) images of jet formation were reported by MacIntyre (1968, 1972) (see original experiments by Kientzler *et al.* (1954)). Interestingly, these studies demonstrated that the surface ripples are created by the retraction of the circular rim of the relaxing bubble cavity. These ripples travel towards the cavity base before the jet emerges. In the words of MacIntyre (1972) (see abstract) '. . . an irrotational solitary capillary ripple precedes the main toroidal rim transporting mass along the surface at approximately 90 % of its phase velocity. The convergence of this flow creates opposed jets . . .'. The seminal work by Duchemin *et al.* (2002) of collapsing bubbles (much smaller than their capillary length scale) at a gas–liquid interface was able to resolve this focussing process, via direct numerical simulations (DNS) of the axisymmetric Navier–Stokes equations without gravity. Figure 1 depicts the generation of an axisymmetric, wavetrain focussing towards the base of the bubble cavity (also the symmetry axis) for two different Ohnesorge numbers (Oh) and at a fixed Bond number (Bo). The Bond number $Bo \equiv \rho^L g \hat{R}_b^2/T$ determines the bubble shape, and the Ohnesorge number $Oh \equiv \mu^L/\sqrt{\rho^L T \hat{R}_b}$ accounts for the ratio of viscous to capillary forces. Here ρ^L, μ^L, T, $\hat{R}_b$ are the lower fluid density, lower fluid viscosity, coefficient of surface tension and equivalent radius of the bubble, respectively. We refer the readers to Deike (2022), Sanjay (2022) and Gordillo & Blanco-Rodríguez (2023) for recent advances on the study of bubble collapse and jet formation mechanisms.

Another example of axisymmetric focussing of surface waves was highlighted in the study by Longuet-Higgins (1990), where several interesting observations were noted. Longuet-Higgins (1990) studied the inverted conical shaped 'impact cavities' seen in experiments and simulations (Oguz & Prosperetti 1990) of a liquid droplet falling on a liquid pool. The author compared these cavities with an exact solution to the potential flow equations without surface tension or gravity (Longuet-Higgins 1983), where the free surface (gas–liquid interface) took the form of a cone at all times. The apex of this cone (i.e. the impact cavity) is often seen to contain a bulge (see figure 2*a* in Longuet-Higgins (1990)) and the formation of this was attributed to (we quote, § 6 first paragraph in Longuet-Higgins (1990)) 'a ripple on the surface of the cone converging towards the axis of symmetry', thus highlighting the role of wave focussing once again. Longuet-Higgins (1990) insightfully remarked that this convergence process would be similar to the radially inward propagation of a circular ripple on a water surface. The interface shape could thus be approximated as being due to the linear superposition of an initial, localised wave packet (generated by distorting an initially flat surface) whose Fourier–Bessel representation $F(k)$ (k being the wavenumber) slowly varies on a time scale $\bar{t}$ (i.e. slow compared with the wave packet propagation time scale t). Longuet-Higgins (1990) thus posits that the shape of the

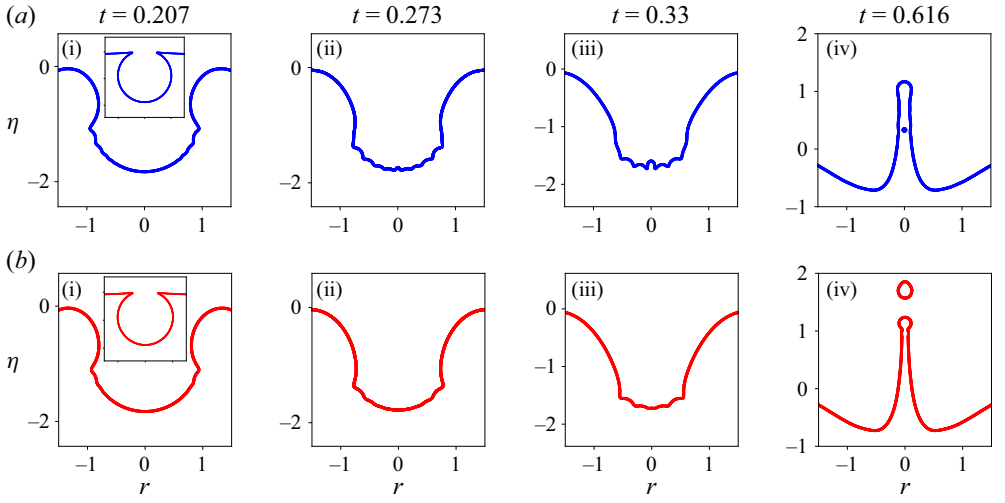

Figure 1. An example of capillary wave focussing obtained from DNS conducted using the open-source code Basilisk (Popinet & Collaborators 2013–2024). The initial cavity shape, inset in (*a* i,*b* i), is obtained by solving the Young–Laplace equation with gravity to determine the shape of a static bubble at the free surface (without its cap). In centimetre–gram–second (CGS) units, initial bubble radius 0.075, surface tension $T = 72$, gravity $g = -981$, density $\rho^L = 1.0$ and $\rho^U = 0.001$ for upper and lower fluid. Panel (*a*) (blue) simulations are conducted using zero viscosity for both gas (above) and liquid (below). Panel (*b*) (red) simulations have dynamic viscosity $\mu^U = 0.0001$ and $\mu^L = 0.01$. Axes are non-dimensionalised using initial bubble radius. Time is non-dimensionalised using the capillary time scale $t = \hat{t}/\sqrt{\rho \hat{R}_b^3/T}$. For panel (*a*) $Bo \equiv \rho^L g \hat{R}_b^2/T = 0.076$ and $Oh = \mu^L/\sqrt{\rho^L T \hat{R}_b} = 0$; for panel (*b*) $Bo = 0.076$ and $Oh = 0.0043$.

perturbed interface $\eta(r, t, \bar{t})$ may be represented as

$$\eta(r, t, \bar{t}) = \int_{\Delta k} F(k, \bar{t}) \mathrm{J}_0(kr) \exp\left(I\sigma(k)t\right) k \, \mathrm{d}k, \tag{1.1}$$

where J_0 is the Bessel function, r is the radial coordinate and the spectrum of the surface perturbation $F(k, \bar{t})$ evolves slowly on a time scale $\bar{t}$, $I \equiv \sqrt{-1}$ and $\sigma(k)$ satisfies the dispersion relation for capillary waves (see equation (6.2) in Longuet-Higgins (1990)). Note that if the slow variation of $F(k, \bar{t})$ over $\bar{t}$ is supressed, (1.1) represents the solution to the linearised Cauchy–Poisson problem with an initial surface distortion whose Hankel transform is $F(k)$. Longuet-Higgins (1990), however, did not report any systematic comparison of available experimental or simulation data (Oguz & Prosperetti 1990) with (1.1) although the author anticipated that nonlinearity could become important during the convergence (see the last paragraph on page 405 of Longuet-Higgins (1990)).

Our current study is partly motivated by the aforementioned observations of Longuet-Higgins (1990) and Duchemin *et al.* (2002) and aims at obtaining an analytical description of spatiotemporal wave focussing at these short scales. We seek an initial, localised surface distortion which produces a wavetrain, and whose radial convergence may be studied analytically, at least in the potential flow limit. We refer the reader to the review by Eggers, Sprittles & Snoeijer (2024) where this limit corresponding to Ohnesorge $Oh = 0$ is discussed. In the next section we present a localised initial surface distortion which is expressible as a linear superposition of Bessel functions (Fourier–Bessel series). It will be seen that this distortion generates a surface wavetrain which focuses towards the symmetry axis of the container. We emphasise that the wavetrains or the solitary ripple seen in Kientzler *et al.* (1954) and Longuet-Higgins (1990), respectively, have

different physical origins compared with the ones we study here. However, following Longuet-Higgins (1990) we intuitively expect there are aspects of their convergence which do not sensitively depend on how these are generated in the first place.

Of particular relevance to us is also the interesting study by Fillette, Fauve & Falcon (2022) who investigated forced capillary–gravity waves in a cylindrical container. These waves were generated via a vertically vibrating ring at the gas–liquid interface. The authors showed that the steady shape of the interface is well represented by the third-order, (nonlinear) time-periodic solution due to Mack (1962). The agreement between the analytical model and experimental data is particularly good around $r = 0$, although differences persist away from the symmetry axis (see their figure 4*b*). With increasing forcing amplitude, the authors note an interesting transition from the linear to the nonlinear regime followed by a jet ejection regime. We demonstrate in Appendix D that a similar transition is also seen for our initial condition (see discussion in the next paragraph) albeit our study excludes external forcing. Due to the absence of forcing, it becomes feasible to carry out a first principles mathematical analysis of the wave-focussing regime, as has been reported here.

While wavetrain convergence and jet formation may often be concomitant, as apparent from the bubble collapse simulations in figure 1, the two phenomena are distinct. Figure 3 of Deike *et al.* (2018), for example, describes experimental investigations of an air bubble bursting at a silicon oil–air interface producing a jet, but without any visible signature of a converging wavetrain towards the collapsing bubble base. On the other hand, the converging wavetrain in the shape oscillations generated due to two coalescing bubbles (Zhang & Thoroddsen (2008); their figure 12), lead to rapid interfacial oscillations at the focal point, but no signature of pinch-off or a liquid jet. When a converging wavetrain and a liquid jet are both present, the dynamics of the latter can be affected by the former quite non-trivially. The fastest jet in such cases can occur at an 'optimal' value of liquid viscosity, rather than in the inviscid limit; see experiments and figure 3(*b*) of Ghabache *et al.* (2014*a*) in the context of bubble bursting. In view of this rather complex aforementioned behaviour, it becomes desirable to have first principles studies of cavity collapse with and without an accompanying wavetrain. The spatially localised interface deformation considered in this study (figure 3), permits access to these phenomena independently, through a tuning parameter. As shown in Appendix D, for small cavity depth (relative to its width), the initial distortion generates a train of radially inward focussed waves (after reflection), which we label as 'wave focussing' and whose physics is of interest here. At larger cavity depth, a jet emerges already at short time due to 'flow focussing'. Notably, this jet is formed significantly before wall reflections can generate a radially inward propagating wavetrain. The study in Basak, Farsoiya & Dasgupta (2021) investigated such a jet, albeit obtained from a single Bessel function. In contrast, we study here the wave focussing regime where no such jet is generated.

As further motivation of our current study, we note that the bubble whose collapse is described in figure 1, is nearly spherical initially as its Bond number is low ($\ll 1$). The highly deformed, multivalued initial shape of such a bubble (inset of figure 1*a* i) precludes expressing it as a Fourier–Bessel series. In contrast, figure 2(*a*) depicts the bubble shape in the converse limit of large Bond number. Here the bubble shape appears like a cavity albeit with sharp protrusions. Such an initial shape (with some smoothing of the protrusions) is amenable to expression in a Fourier–Bessel series, whose coefficients may be evaluated in time. The cavity treated in this study, may thus be considered a crude approximation to a bubble at high Bond number. For numerical reasons, we have chosen our initial deformation to be a cavity with smooth humps (see figure 3) in contrast to the bubble shape

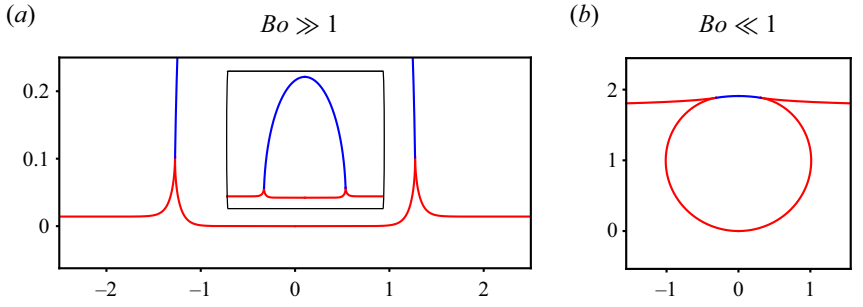

Figure 2. The effect of change of Bond number on the shape of a static bubble. (*a*) The bubble shape for $Bo = 222 \gg 1$. (*b*) An air bubble corresponding to $Bo = 0.076 \ll 1$, also see inset in figure 1(*a*). As the Bond number is increased, an increasingly larger fraction of the bubble shifts upwards (compared with the mean interface level at large distance) and its 'rim', see sharp corners in (*b*), distorts into vertically pointing kinks seen in (*a*). For $Bo \gg 1$, the bubble shape is a single-valued function $\eta(r)$, the red curve in (*a*), and provides the motivation for the initial interface distortion (albeit significantly smoother) in figure 3 and treated analytically in this study. The curves in blue in (*a*,*b*) represent the bubble cap. The inset in (*a*), depicts the entire bubble including its cap while the main figure, highlights the bubble 'rim'.

with kinks in figure 2(*a*). We emphasise that for such an initial deformation as studied here, the physical origin of the focussing wave train that appears in our simulations is different from that of Gordillo & Rodríguez-Rodríguez (2019). Consequently, the focussing of the wavetrain is not the same as that of the wavetrain in classical bursting of bubbles at low *Bo*. However, qualitative similarities in certain aspects may be expected between the two situations and are studied here (see Appendix E).

We develop an inviscid nonlinear theory for the focussing of a concentric wavetrain resulting from the aforementioned *a priori* imposed free-surface deformation. This theory developed from first principles here has no fitting parameters and helps delineate those aspects of focussing which may be accounted for by linear theory compared with nonlinear features. In a series of earlier theoretical and computational studies from our group (Farsoiya, Mayya & Dasgupta 2017; Basak *et al.* 2021; Kayal, Basak & Dasgupta 2022; Kayal & Dasgupta 2023), we have solved the initial-value problem corresponding to delocalised, initial interface distortions in the form of a single Bessel function ($J_0(kr)$) at gravity-dominated large scales (Kayal & Dasgupta 2023), gravito–capillary intermediate scales (Farsoiya *et al.* 2017; Basak *et al.* 2021) and capillarity-dominated small scales (Kayal *et al.* 2022) (also see the recent study in Dhote *et al.* (2024) for a delocalised initial perturbation on a sessile bubble). In contrast to these studies where the initial perturbation was spatially delocalised, we study here a spatially localised initial excitation. Apart from the obvious advantage of easier experimental realisation of this (see Ghabache, Séon & Antkowiak (2014*b*) for experiments at gravity dominated scales), this initial condition has the additional advantage that already at linear order, a radially propagating concentric wavetrain is obtained and one can ask how does this converge at the axis of symmetry? In contrast, for the single Bessel function initial excitation as in Basak *et al.* (2021), Kayal *et al.* (2022) and Kayal & Dasgupta (2023), at linear order one obtains only a standing wave and it is necessary to proceed to quadratic order and beyond to generate the focussing wavetrain.

The manuscript is structured as follows. Section 2 illustrates the time evolution of a relaxing cavity and introduces the analytical equations for wave evolution. Section 3 compares these analytical results with DNS. Finally, the paper culminates with discussions and outlook in § 4.

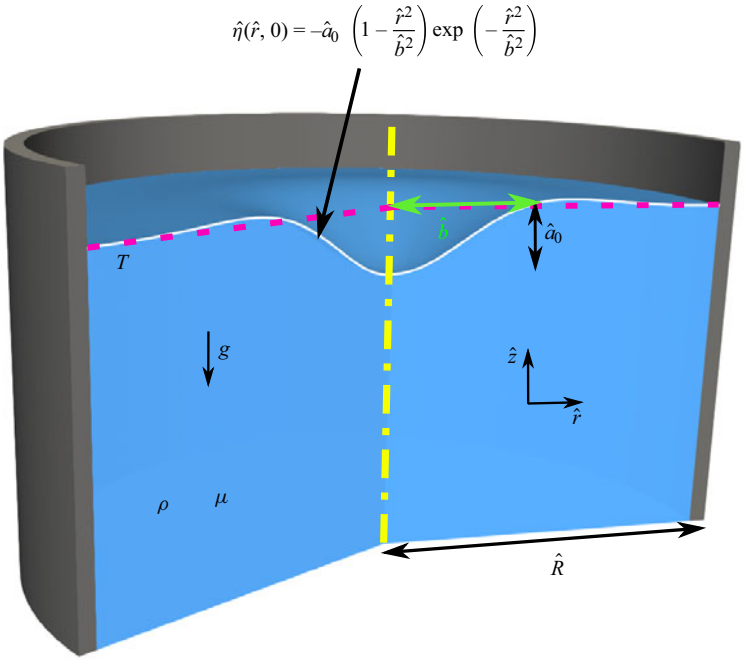

Figure 3. A (not to scale) cross-sectional representation of the initial interface distortion $\hat{\eta}(\hat{r}, 0)$ shaped as a cavity of half-width $\hat{b}$ and depth $\hat{a}_0$ in a cylinder of radius $\hat{R}$ filled with liquid (in blue). The functional form chosen for $\hat{\eta}(\hat{r}, 0)$ was first proposed by Miles (1968) and represents a volume preserving distortion on radially unbounded domain. The red dotted line indicates the unperturbed level of the free surface of the liquid pool. The gas–liquid surface tension is T. Liquid density and viscosity are ρ and μ, respectively, g is gravity. The cavity shape can be considered as a crude representation to the $Bo \gg 1$ bubble shape in figure 2 with the kinks smoothened drastically. It must be emphasised that our initial condition and the resulting wavetrain are significantly different from that of a bursting bubble. However, we intuitively expect that there may be qualitative similarities between the two processes and that it is possible to learn something about one by studying the other, which incidentally has the advantage of analytical tractability.

2. Time evolution of a relaxing cavity

As shown in figure 3, the system consists of a cylindrical container of radius $\hat{R}$ filled with quiescent liquid (indicated in blue). As we do not model the upper fluid in our theory, here onwards the superscript L is dropped from the variables representing fluid properties. For simplicity of analytical calculation, the cylinder is assumed to be infinitely deep and the gas–liquid density ratio is kept fixed at 0.001 for DNS only. In our theoretical calculations, we approximate the gas–liquid interface as a free surface and neglect any motion in the gas phase (although, it is modelled in our DNS). Some of the relevant length scales are the gravito–capillary length $l_c \equiv \sqrt{T/\rho g} \approx 2.7\,\text{mm}$ and the viscocapillary length scale $l_\mu \equiv \mu^2/\rho T \approx 0.01\,\mu\text{m}$. For our chosen half-width of the initial interface perturbation ($\hat{b} = 8.0\,\text{mm}$), these length scales justify the inclusion of both capillarity as well as gravity in the theoretical calculation while neglecting viscosity at the leading order. However, we stress that viscosity is known to have a non-monotonic effect on wave focussing in a collapsing bubble, as demonstrated by Ghabache *et al.* (2014*a*). Their figure 3 shows that the jet velocity during bubble bursting varies non-monotonically with increasing viscosity. Thus, the fastest jets occur not in an inviscid system but at an 'optimal' viscosity. In what follows, we employ potential flow equations in our theory and do not treat the boundary

layers expected to be generated at the air–water interface and the cylinder walls (Mei & Liu 1973). We will address the inclusion of viscous effects later in the study.

Before delving into the theoretical formulation, it is instructive to discuss the phenomenology of the problem. Figure 4(*a–i*) depict the interface at various time instants as obtained from DNS. These are obtained by solving the inviscid, axisymmetric and incompressible Euler's equations with surface tension and gravity in cylindrical coordinates (Basilisk, Popinet & Collaborators 2013–2024) (a script file is available as Supplementary material (Kayal 2024)). The images in figure 4 are obtained by generating the surface of revolution of axisymmetric DNS data. As shown in figure 4(*a*), the interface is initially distorted in the shape of an axisymmetric, stationary and localised perturbation. As this cavity relaxes, waves are generated which travel outward reflecting off the wall (between figure 4*e* and figure 4*f*). This produces a wavetrain which focusses at the symmetry axis of the container ($r = 0$). One notes the formation of a small dimple-like structure at the symmetry axis in figure 4(*h*). In § 3, we will demonstrate that neither the dimple nor other interface features around the symmetry axis can be explained by the linear theory.

2.1. *Governing equations: potential flow*

We now turn to the theoretical analysis of the phenomenology illustrated in figure 4. In the base state, we consider a quiescent pool of liquid with density ρ and surface tension T contained in a cylinder of radius $\hat{R}$. For analytical simplicity, we assume this pool is infinitely deep compared with the wavelength of the excited interface waves. For further simplicity, we assume that the solid–liquid contact angle at the cylinder wall is always fixed at $\pi/2$ and the contact line is free to move ($\partial_n v_t = 0$). This is the simplest contact line condition which allows for reflection of waves at the boundary without complicating the analytical treatment of the problem (Snoeijer & Andreotti 2013). The variables $\hat{\eta}(\hat{r}, \hat{t})$ are used to represent the axisymmetric perturbed interface (see figure 1) and $\hat{\phi}(\hat{r}, \hat{z}, \hat{t})$ is the disturbance velocity potential; $\hat{r}$ and $\hat{z}$ being the radial and axial coordinates in cylindrical geometry, respectively. Variables with the dimensions of length (e.g. $\hat{r}, \hat{z}, \hat{\eta}$) and time ($\hat{t}$) are scaled using length and time scales $L \equiv \hat{R}$ and $T_0 \equiv \sqrt{\hat{R}/g}$, respectively. The velocity potential $\hat{\phi}$ is non-dimensionalised using the scale L^2/T_0. Under the potential flow approximation, the non-dimensional governing equations and boundary conditions governing perturbed quantities are

$$\frac{\partial^2 \phi}{\partial r^2} + \frac{1}{r}\frac{\partial \phi}{\partial r} + \frac{\partial^2 \phi}{\partial z^2} = 0, \tag{2.1a}$$

$$\frac{\partial \eta}{\partial t} + \left(\frac{\partial \eta}{\partial r}\right)\left(\frac{\partial \phi}{\partial r}\right)_{z=\eta} - \left(\frac{\partial \phi}{\partial z}\right)_{z=\eta} = 0, \tag{2.1b}$$

$$\left(\frac{\partial \phi}{\partial t}\right)_{z=\eta} + \eta + \frac{1}{2}\left\{\left(\frac{\partial \phi}{\partial r}\right)^2 + \left(\frac{\partial \phi}{\partial z}\right)^2\right\}_{z=\eta} - \frac{1}{Bo}\left\{\frac{\dfrac{\partial^2 \eta}{\partial r^2}}{\left\{1 + \left(\dfrac{\partial \eta}{\partial r}\right)^2\right\}^{3/2}} + \frac{1}{r}\frac{\dfrac{\partial \eta}{\partial r}}{\left\{1 + \left(\dfrac{\partial \eta}{\partial r}\right)^2\right\}^{1/2}}\right\} = 0, \tag{2.1c}$$

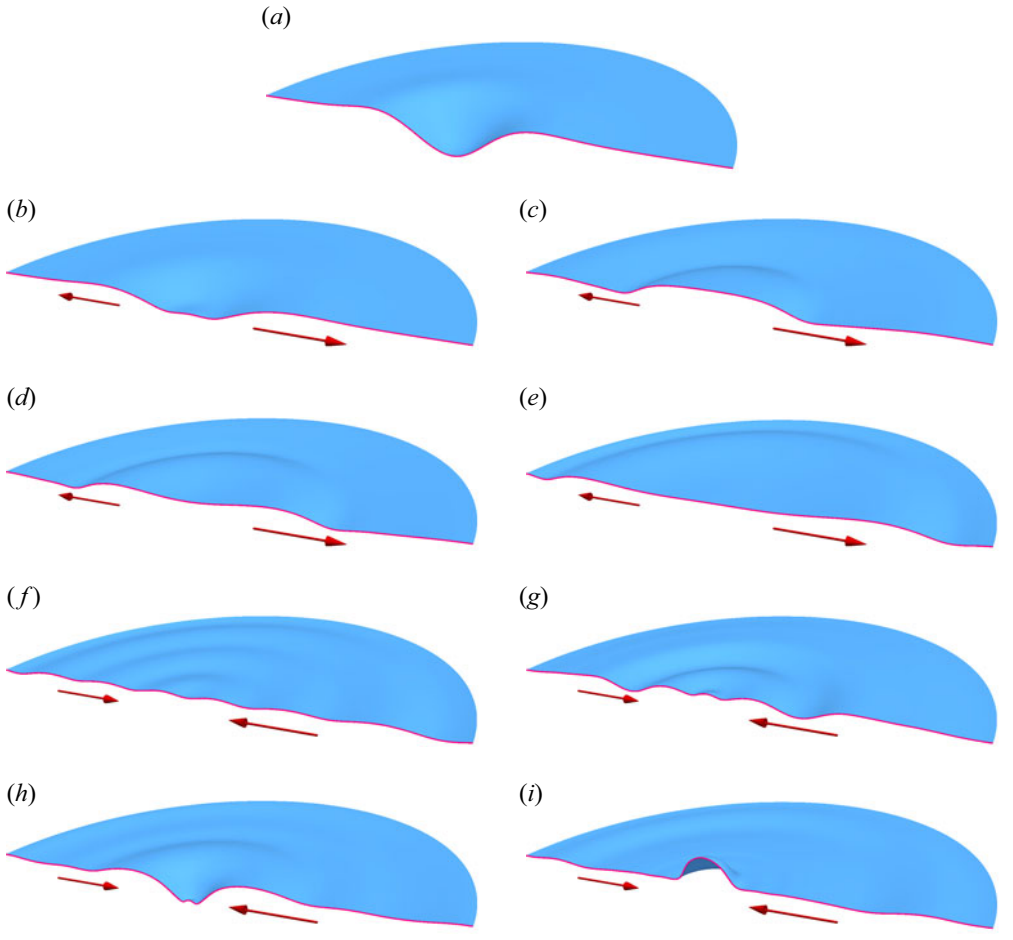

Figure 4. Wave focussing observed in DNS from the cavity-shaped interface distortion at $t = 0$ *a*). The figure is to be read from left to right and top to bottom for the progression of time. After the waves reflect off the cylinder wall (between panels (*e*) and (*f*); the confining walls are not shown), they focus inwards towards $r = 0$ producing strongly nonlinear oscillations of increasing amplitude. The arrows indicate the instantaneous direction of wave motion. The DNS parameters may be read from Case 1 in table 1.

$$\int_0^1 r\eta(r,t)\,\mathrm{d}r = 0, \quad \left(\frac{\partial\phi}{\partial r}\right)_{r=1} = 0, \tag{2.1d,e}$$

$$\lim_{z\to-\infty}\phi \to \text{finite} \tag{2.1f}$$

$$\eta(r,t=0) = -\varepsilon\left(1-\frac{r^2}{b^2}\right)\exp\left(-\frac{r^2}{b^2}\right) = \sum_{m=1}^{N}\eta_m(0)\mathrm{J}_0(k_m r),$$

$$\frac{\partial\phi}{\partial n}(r, z=\eta(r,0), t=0) = 0, \tag{2.1g,h}$$

where $\varepsilon > 0$ and n in (2.1*h*) is a distance coordinate measured normal to the free surface at $t = 0$. The dimensionless parameters are defined as follows: $1/Bo \equiv \alpha \equiv T/\rho g\hat{R}^2$, representing the inverse Bond number (based on the cylinder radius); $b \equiv \hat{b}/\hat{R}$ is the

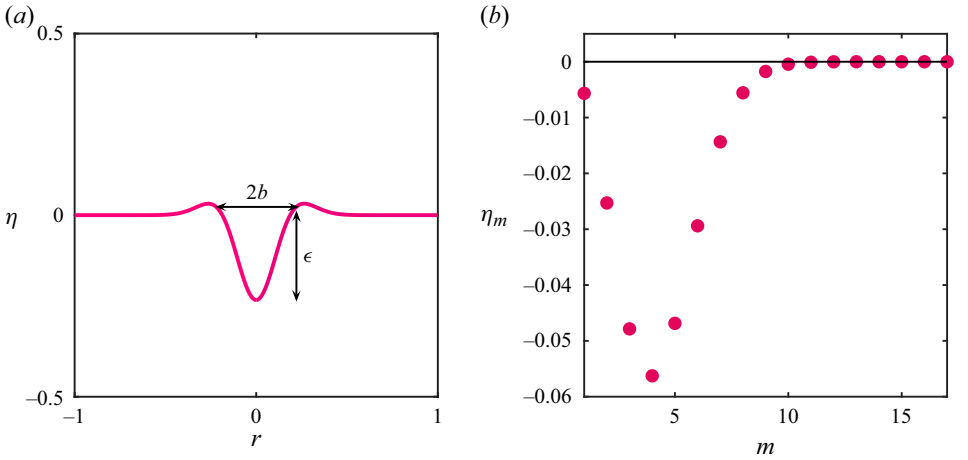

Figure 5. (*a*) The gas–liquid interface initially deformed as a cavity of half-width $b = \hat{b}/\hat{R}$ and depth $\varepsilon \equiv \widehat{a_0}/\hat{R}$ (cavity shape at $t = 0$). (*b*) The coefficients $\eta_m(0)$ are obtained by decomposing the initial distorted interface. For this initial distortion, $\varepsilon = 0.091, b = 0.187$. It is seen that only the first 10 or so Bessel functions/wavenumbers are excited initially (Bessel function coefficients). For accuracy, we consider the energy in the first seventeen initially ($m = 1, 2, 3, \ldots, 17$).

dimensionless measure of cavity width; and $\varepsilon \equiv \hat{a}_0/\hat{R}$ is the dimensionless measure of cavity depth (see figure 3 caption for the meaning of the symbols). Here onwards, we use α to represent the inverse Bond number.

In cylindrical, axisymmetric coordinates (2.1*a*) is the Laplace equation, (2.1*b*) and (2.1*c*) are the kinematic boundary condition and the Bernoulli equation applied at the free surface, respectively. Equation (2.1*d*) restricts initial interfacial distortions to those which are volume conserving while (2.1*e*) enforces no-penetration at the cylinder wall. Equation (2.1*f*) is the finiteness condition at infinite depth.

Equation (2.1*g*,*h*) represent the initial conditions. We decompose the initial interface distortion, i.e. $\eta(r, t = 0) = -\varepsilon(1 - r^2/b^2)\exp(-(r^2/b^2))$ (Miles 1968), into its Fourier–Bessel series as indicated by the second equality sign in (2.1*g*) and $\mathrm{J}_1(k_m) = 0$ for $m \in \mathbb{Z}^+$ (from (2.1*e*); note the identity $\mathrm{J}_0'(\cdot) = -\mathrm{J}_1(\cdot)$, the prime indicating a derivative). The numerical values of the coefficients η_m at $t = 0$, i.e. $\eta_m(0)$ ($m = 1, 2, 3, \ldots$) in (2.1*g*) are determined from the orthogonality relation between Bessel functions, i.e. $\eta_m(0) = \int_0^1 \mathrm{d}r\, r\mathrm{J}_0(k_m r)\eta(r, 0)/\int_0^1 \mathrm{d}r\, r\mathrm{J}_0^2(k_m r)$. A sample representation of the initial condition and its Fourier–Bessel coefficients is presented in figures 5(*a*) and 5(*b*), respectively, where it is seen that approximately 17 wavenumbers are excited initially. Subject to these initial and boundary conditions presented in (2.1*a–h*), we need to determine the amplitudes $\eta_m(t)$, $m = 1, 2, 3 \ldots$ as a function of time and this is carried out next.

2.2. *Equations for* $\eta_j(t)$

In this section we solve the initial, boundary-value problem posed in (2.1*a–h*). We derive equations governing the time evolution of the coefficients $\eta_j(t)$ up to quadratic order (i.e. terms which are cubic or higher in the coefficients are neglected). The approach for doing this is classical and was laid out in Hasselmann (1962) in Cartesian coordinates although their initial conditions were random functions in contrast to the deterministic initial distortion posed in (2.1*g*). The procedure below closely follows the approach of

Nayfeh (1987), who derived similar equations (his equations (14) and (15)) in the context of the Faraday instability (i.e. with vertical oscillatory forcing) including gravity but not surface tension (Nayfeh 1987) in his analysis. In contrast to forced waves being studied by Nayfeh (1987), we consider free waves in our current study and include both surface tension and gravity in the analysis. We first expand ϕ and η in (2.1) as

$$\phi(r,z,t)=\sum_{m=1}^{\infty}\phi_m(t)\mathrm{J}_0(k_m r)\exp(k_m z),\quad \eta(r,t)=\sum_{m=1}^{\infty}\eta_m(t)\mathrm{J}_0(k_m r). \tag{2.2a,b}$$

By construction, each term in the expansion in (2.1) satisfies the Laplace equation (2.1*a*), (2.1*d*) (the integral mass conservation condition evaluates to be numerically very small for the chosen parameters) and (2.1*e*) as well as the finiteness condition (2.1*f*). Taylor expanding (2.1*b*) and (2.1*c*) about $z=0$ we obtain

$$\frac{\partial\eta}{\partial t}-\left(\frac{\partial\phi}{\partial z}\right)_{z=0}-\left(\frac{\partial^2\phi}{\partial z^2}\right)_{z=0}\eta+\frac{\partial\eta}{\partial r}\left(\frac{\partial\phi}{\partial r}\right)_{z=0}+\text{H.O.T}=0, \tag{2.3a}$$

$$\left(\frac{\partial\phi}{\partial t}\right)_{z=0}+\eta\left(\frac{\partial^2\phi}{\partial t\partial z}\right)_{z=0}+\eta+\frac{1}{2}\left\{\left(\frac{\partial\phi}{\partial r}\right)^2+\left(\frac{\partial\phi}{\partial z}\right)^2\right\}_{z=0}-\alpha\left\{\frac{\partial^2\eta}{\partial r^2}+\frac{1}{r}\frac{\partial\eta}{\partial r}\right\}+\text{H.O.T}=0 \tag{2.3b}$$

where H.O.T represents higher-order terms. Substituting expansions (2.2*a*,*b*) into (2.3*a*,*b*) and using orthogonality relations between Bessel functions we obtain for $n,p,m\in\mathbb{Z}^+$ the following:

$$\frac{\mathrm{d}\eta_n}{\mathrm{d}t}-k_n\phi_n(t)+\sum_{m,p}\left(D_{npm}-k_m^2C_{npm}\right)\phi_m(t)\eta_p(t)=0, \tag{2.4a}$$

$$\frac{\mathrm{d}\phi_n}{\mathrm{d}t}+\left(1+\alpha k_n^2\right)\eta_n(t)+\sum_{m,p}k_mC_{npm}\left(\frac{\mathrm{d}\phi_m}{\mathrm{d}t}\right)\eta_p(t)+\frac{1}{2}\sum_{m,p}\left(D_{npm}+k_mk_pC_{npm}\right)\phi_m(t)\phi_p(t)=0$$
$$n=1,2,3\ldots. \tag{2.4b}$$

The nonlinear interaction coefficients C_{npm} and D_{npm} in (2.4) are related as (Nayfeh 1987)

$$D_{npm}=\frac{1}{2}\left(k_p^2+k_m^2-k_n^2\right)C_{npm} \tag{2.5}$$

and $C_{npm}=\int_0^1 r\mathrm{J}_0(k_nr)\mathrm{J}_0(k_pr)\mathrm{J}_0(k_mr)\,\mathrm{d}r/\int_0^1 r\mathrm{J}_0^2(k_nr)\,\mathrm{d}r$. For the benefit of the reader, the detailed proof of (2.5) is provided in Appendix A. Retaining self-consistently up to quadratic-order terms, (2.4*a*) and (2.4*b*) may be combined into a second-order equation

for η_n alone. This is

$$\frac{\mathrm{d}^2\eta_n}{\mathrm{d}t^2} + \omega_n^2\eta_n + k_n \sum_{m,p} \left[1 + \frac{k_p^2 - k_m^2 - k_n^2}{2k_m k_n}\right] C_{npm} \left(\frac{\mathrm{d}^2\eta_m}{\mathrm{d}t^2}\right) \eta_p$$
$$+ \frac{1}{2} k_n \sum_{m,p} \left[1 + \frac{k_p^2 + k_m^2 - k_n^2}{2k_m k_p} + \frac{k_p^2 - k_m^2 - k_n^2}{k_m k_n}\right] C_{npm} \left(\frac{\mathrm{d}\eta_m}{\mathrm{d}t}\right)\left(\frac{\mathrm{d}\eta_p}{\mathrm{d}t}\right) = 0. \tag{2.6}$$

Note that ω_n is the linear oscillation frequency of the nth mode, *viz.* $\omega_n \equiv \sqrt{k_n(1 + \alpha k_n^2)}$ (the effect of the nonlinear terms due to curvature in (2.3*b*) and thus surface tension, appears only through the linear-order dispersion relation up to second order). We solve the coupled ordinary differential equation (ODE) (2.6) numerically subject to the initial conditions discussed earlier for $n = 1, 2, 3, \ldots 34$ (i.e. twice the initial number, see figure 5*b*) using 'DifferentialEquations.jl', an open-source package by Rackauckas, Nie & Collaborators (2017) and collaborators. The 'DifferentialEquations.jl' automatically chooses an ODE solver based on stiffness detection algorithms as described by Rackauckas & Nie (2019). The Julia script file can be found in Kayal (2024). We note that while numerically solving (2.6), we compute $\mathrm{d}^2\eta_m/\mathrm{d}t^2$ in the third term of the equation (the nonlinear term) via the linear estimate, *viz.*, $\mathrm{d}^2\eta_m/\mathrm{d}t^2 = -\omega_m^2\eta_m$. Interestingly, the solution to (2.6) shows instability albeit only at large time (compared with the focussing time) when high wavenumbers (k) appear in our model. This instability could either be numerical or physical and possibly related to instability of finite-amplitude capillary waves. Further investigations are necessary to ascertain the origin of this and is outside the scope of this study. As the instability occurs outside the time window of our study, it does not impact the results presented in this work. We thus restrict ourselves to numerical solutions to (2.6) within the time period of our interest where this instability does not appear.

As benchmarking of our numerical solution procedure, we first solve (2.6) employing the single Bessel function initial surface distortion that was studied in Basak *et al.* (2021), i.e. in our current notation $\eta(r, t = 0) = \varepsilon \mathrm{J}_0(l_5\, r),\ \varepsilon > 0$ where $l_5 = 16.4706$ is the fifth non-trivial root of the Bessel function J_1. For this initial condition, the second-order accurate solution is expectedly of the form

$$\eta(r, t) = \varepsilon\eta_1(r, t) + \varepsilon^2\eta_2(r, t), \tag{2.7}$$

where explicit expressions for η_1 and η_2 were provided in Basak *et al.* (2021) (we note the slight difference in non-dimensionalisation of length between the current study and the one by Basak *et al.* (2021) involving a factor of l_q). Figure 6 demonstrates a comparison between the prediction of (2.7) (indicated in the figure as 'B21' for Basak *et al.* (2021)), the solution obtained from solving (2.6) with the same initial condition (labelled in the figure as 'analytical') and the numerical simulation from Basilisk (depicted as 'simulation'). Figure 6 demonstrates good agreement between the three, thereby providing confidence on our numerical procedure for solving (2.6).

3. Comparison of DNS with theory

3.1. *Description*

We have used the open-source code Basilisk (Popinet & Collaborators 2013–2024) to solve the Navier–Stokes equation with an interface *viz.*

$$\boldsymbol{\nabla} \cdot \boldsymbol{u} = 0, \tag{3.1}$$

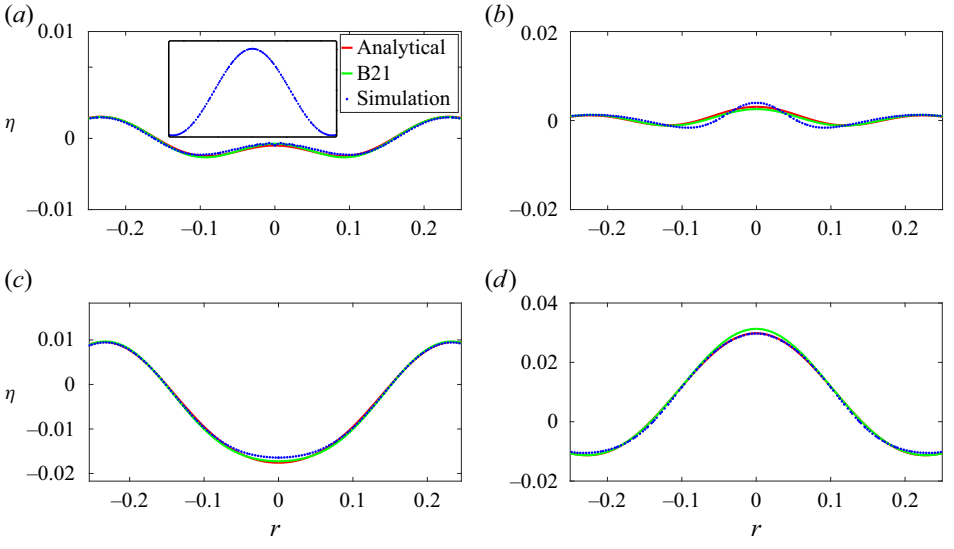

Figure 6. Benchmarking of our solution procedure for solving the coupled ODEs in (2.6) against inviscid DNS (indicated as 'simulation' in the legend of panel (*a*)) and analytical predictions by Basak *et al.* (2021), indicated as 'B21'. For DNS, the dimensionless parameters are $\varepsilon \equiv a_0/\hat{R} = \frac{0.5}{16.4706} = 0.03$, $\alpha = 0.004$ and $Oh = 0$. Note that the initial condition here has a crest around $r = 0$, see the inset of panel (*a*). Here (*a*) $t = 0.303$; (*b*) $t = 0.409$; (*c*) $t = 0.772$; (*d*) $t = 1.029$.

$$\frac{\partial \boldsymbol{u}}{\partial t} + \boldsymbol{\nabla} \cdot (\boldsymbol{u} \bigotimes \boldsymbol{u}) = -\frac{\boldsymbol{\nabla} p}{\rho} + g + \frac{T}{\rho}\kappa \delta_s \boldsymbol{n} + \nu \nabla^2 \boldsymbol{u}, \tag{3.2}$$

$$\frac{\partial f}{\partial t} + \boldsymbol{\nabla} \cdot (f \boldsymbol{u}) = 0. \tag{3.3}$$

Here, $\boldsymbol{u}, p, \kappa, T$ and f are the velocity field, pressure field, interface curvature, surface tension and the colour-function field, respectively. Basilisk is a one-fluid solver where the colour function f takes values 0 and 1 in the two phases with the interface being represented geometrically using the volume-of-fluid algorithm in cells where $0 < f < 1$. The density and viscosity are represented as a weighted average of the respective values of the two phases, employing the colour function as the weight. Figure 7 depicts the simulation domain, the wall labelled 1 is the symmetry axis, and the liquid and gas are indicated in different colours. We have solved (3.1), (3.2) and (3.3) numerically in cylindrical axisymmetric coordinates, using an adaptive mesh based on temporal changes of the colour function f, and velocity $\boldsymbol{u}$. Grid resolution for different cases are provided in table 1. In all the viscous simulations treated in the manuscript, we have used free-slip walls with a 90° contact angle, in order to be compatible with a freely moving contact line and obviate the well-known contact line singularity (Snoeijer & Andreotti 2013). By using free-slip conditions, we maintain consistency with the analytical expressions used in our study and facilitate a more direct comparison between our numerical results and theoretical predictions. This boundary condition naturally enforces a 90° contact angle at the wall, setting a vanishing gradient for the colour function close to the wall, which is consistent with the assumptions in the theoretical model far from the centre of the cavity. For discussions, we refer to Wildeman *et al.* (2016) which shows that the free-slip condition with a 90° contact angle effectively eliminates dissipation close to the contact line, allowing us to focus on the interfacial dynamics that are central to our study.

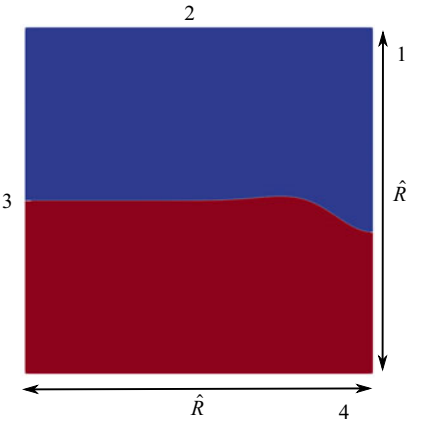

Figure 7. Simulation domain. Only half of the domain is depicted, due to the axis of symmetry (side labelled 1). For both viscous as well as inviscid simulations, the boundaries labelled 2, 3 and 4 are modelled as free-slip walls.

3.2. *Comparison*

In this section, we compare results from our DNS with the theory discussed in § 2. Before this, it is instructive to rationalise the reflection process and estimate its duration. To do this, we observe that the Fourier–Bessel spectrum of the initial interface distortion prominently features a peak at $m = 4$ (see figure 5*b*). A rough estimate of the time required for the energy associated with any wavenumber excited in the initial spectrum to complete a return trip (from $\hat{r} = 0$ to the wall and back) can be derived from linear theory. When this return time is estimated for the dominant wavenumber in the initial spectrum, we expect the numerical value to roughly coincide with the generation time of the largest amplitude oscillation at $\hat{r} = 0$ during the focussing process. This is illustrated in figure 8, where the time signal from tracking the interface at $\hat{r} = 0$ is presented (Case 2 in table 1). Note that this figure uses dimensional variables, denoted with hats. After the outward travelling waves move away, the interface at $\hat{r} = 0$ remains relatively quiescent, as indicated by the nearly flat time signal around $\hat{t} = 0.2$ s. As a result of reflection, the energy associated with every wavenumber k present initially focusses back to $\hat{r} = 0$, this return trip is carried out with its group velocity $\hat{c}_g = (g + 3(T/\rho)k^2)/(2\sqrt{gk + Tk^3/\rho})$. In figure 5(*b*), the dominant wavenumber is $k_d = l_4/\hat{R}$ and the largest oscillation at $\hat{r} = 0$ during the focussing process is seen to be generated at $\hat{t}_{peak} = 0.384$ s from figure 8. Using the linear estimate $\hat{t}_{peak} \approx 2\hat{R}/\hat{c}_{gd}$ where $\hat{c}_{gd}$ is the group velocity of the dominant wavenumber, we obtain the value 0.403 s which is reasonably close to the observed $\hat{t}_{peak} = 0.384$ s.

In the collage of images in figures 9 and 10, we present the shape of the interface as a function of time for Cases 1 and 2 in table 1, respectively, comparing this with linear and nonlinear theoretical predictions. The only difference between these two figures is in the value of ε, all other dimensionless numbers remaining the same. Here linear theory implies solution to (2.6) without the nonlinear terms. Note that this is equivalent to superposition of the form $\eta(r, t) = \sum_{m=1}^{17} \eta_m(0) \mathrm{J}_0(k_m r) \cos(\omega_m t)$ where $\omega_m(k_m)$ satisfies the gravito–capillary dispersion relation for deep water. In figure 9, the transition from outward propagating waves to inward propagating ones occur between figure 9(*c*) and figure 9(*d*). For figure 9(*a*), figure 9(*b*) and figure 9(*c*) it is evident that linear theory represents the outgoing waves accurately. However, as focussing commences from

Case	$\varepsilon \equiv \dfrac{\hat{a}_0}{\hat{R}}$	$Oh \equiv \dfrac{\mu}{\sqrt{\rho T \hat{b}}}$	$\hat{a}_0$	μ	Grid (maximum)
1	0.061	0	0.26	0	10
2	0.091	0	0.39	0	9, 10, 11
3	0.091	1.17×10^{-5}	0.39	8.9×10^{-5}	10
4	0.091	1.17×10^{-4}	0.39	8.9×10^{-4}	9, 10, 11
5	0.091	1.17×10^{-3}	0.39	8.9×10^{-3}	10
6	0.091	1.17×10^{-2}	0.39	8.9×10^{-2}	10
7	0.006	0	0.026	0	
8	0.006	1.17×10^{-5}	0.026	8.9×10^{-5}	10
9	0.006	1.17×10^{-4}	0.026	8.9×10^{-4}	10
10	0.006	1.17×10^{-3}	0.026	8.9×10^{-3}	10
11	0.006	3.7×10^{-3}	0.026	2.81×10^{-2}	10
12	0.006	1.17×10^{-2}	0.026	8.9×10^{-2}	10
13	0.091	2.34×10^{-4}	0.39	1.78×10^{-3}	10
14	0.091	4.68×10^{-4}	0.39	3.56×10^{-3}	10
15	0.091	2.92×10^{-6}	0.39	2.22×10^{-5}	10
16	0.091	5.85×10^{-6}	0.39	4.45×10^{-5}	10

Table 1. All dimensional lengths are indicated with a hat. Values are quoted in CGS units. In all of the cases we have used $\hat{R} = 4.282$ cm, $\hat{b} = 0.8$ cm, $T = 72$ dyne cm^{-1}, $g = -981$ cm s^{-2}, $\rho = 1$ gm cm^{-3}. These imply dimensionless values $b \equiv \hat{b}/\hat{R} = 0.187$, $\alpha \equiv T/\rho g \hat{R}^2 = 0.004$. Here Oh has been defined using $\hat{b}$, in order to be comparable to its value for a bursting bubble where radius of the bubble is considered for defining Oh. One may obtain a new Ohnesorge number Oh' based on $\hat{R}$ by using the formulae $Oh' \equiv \mu/\sqrt{\rho T \hat{R}} = Oh \times b^{1/2}$ with $b \equiv \hat{b}/\hat{R}$. The maximum grid resolution reported here are in powers of two. The conditions for adaptivity may be found in further detail in the script files (Kayal 2024).

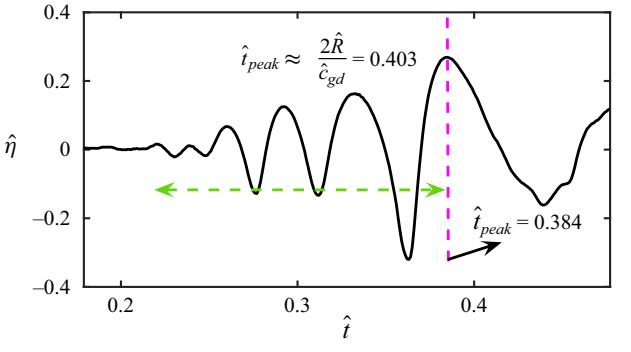

Figure 8. Time signal of the interface at $\hat{r} = 0$. The green line indicates approximately the time window when focussing takes place at $\hat{r} = 0$.

figure 9(*d*) onwards, we notice significant differences between linear theory and (inviscid) DNS. Interestingly, second-order theory seems to predict the shape of the interface around $r = 0$ quite well. Figure 10 shows a more intense scenario than figure 9, featuring a larger $\varepsilon = 0.091$. The transition from predominantly linear to nonlinear behaviour occurs between figure 10(*c*) and figure 10(*d*), representing outgoing and incoming waves, respectively. Notably, sharp dimple-like structures emerge around $r = 0$, as seen in figure 10(*h*), which are well described by nonlinear theory. Additionally, the tendency to

form jets (although no clear jet is visible), as seen in figure 10(*j*), is noteworthy, although the nonlinear theory is only qualitatively accurate in this context. We refer the reader to the accompanying Supplementary Movie 1 available at https://doi.org/10.1017/jfm.2024.1089 ($\varepsilon = 0.061$) and Movie 2 ($\varepsilon = 0.091$), see additional Supplementary material which visualises these.

3.3. *Role of nonlinearity at $r = 0$*

Figures 9 and 10 show that although the linear solution is a reasonable model for the interface evolution before reflection, it shows deviation from the fully nonlinear simulation at the axis of symmetry during radial convergence of the wavetrain. Towards understanding this better, we provide two sets of analysis in the following subsections. In § 3.3.1, we analyse the time-periodic solution by Mack (1962), investigating the role of nonlinearity generated bound components around $r = 0$. In § 3.3.2, we analyse the initial deformation as a Bessel function, akin to Basak *et al.* (2021). It will be seen from both analysis that bound components play an important role in the interface deformation around $r = 0$.

3.3.1. *Comparison with time-periodic solution*

Unlike the initial interface distortion studied so far which leads to aperiodic behaviour, there also exist finite-amplitude deformations which generate time-periodic oscillations. Such finite-amplitude, time-periodic solutions are the standing-wave counterparts of the well-known Stokes travelling wave. In rectangular coordinates, such a standing-wave solution was first developed by Rayleigh (Strutt 1915) and in further detail by Penney *et al.* (1952). This was extended to radially bounded, cylindrical geometry for finite liquid depth in Mack (1962). In the deep-water limit, Mack's solution contains three parameters, all appearing in the 'free wave' (see below) part of the solution represented by $\tilde{a}_0 \mathrm{J}_0(k_q \hat{r}/\hat{R})$, $q = 1, 2, 3, \ldots$. These in turn lead to two non-dimensional parameters *viz.* $\tilde{\epsilon} \equiv \tilde{a}_0/\hat{R}$ and a positive integer $q = 1, 2, 3, \ldots$ specifying the number of zero crossings of J_0 within the radial domain, a measure of crest-to-crest distance of the perturbation (J_0 is not periodic but becomes so asymptotically). In non-dimensional form the time-periodic solution of Mack (1962) may be written as

$$\eta(r, \tilde{t}; \tilde{\epsilon}, q) = T_0(r; \tilde{\epsilon}, q) + T_1(r; \tilde{\epsilon}, q)\cos(2\pi\tilde{t}) + T_2(r; \tilde{\epsilon}, q)\cos(4\pi\tilde{t}) + T_3(r; \tilde{\epsilon}, q)\cos(6\pi\tilde{t}), \tag{3.4}$$

where $\tilde{t} \equiv \omega\hat{t}/2\pi$. Mack (1962) obtained expressions for $T_0(r)$, $T_1(r)$ and $T_2(r)$ for $q = 1$ employing $\tilde{\epsilon}$ as perturbative parameter (up to $O(\tilde{\epsilon}^3)$) and expressions for these along with the nonlinear frequency $\omega(\tilde{\epsilon}, q = 1)$ are provided in Appendix A, adapted to our notation.

Note that the solution by Mack (1962) excludes capillary effects. Referring to Appendix A, we note that $T_0(r)$ is of $O(\tilde{\epsilon}^2)$ while $T_1(r)$, $T_2(r)$ and $T_3(r)$ are of $O(\tilde{\epsilon})$, $O(\tilde{\epsilon}^2)$ and $O(\tilde{\epsilon}^3)$, respectively. As a first step, we evaluate the accuracy of (3.4) at a relatively high steepness of $\tilde{\epsilon} \approx 0.16703$. This value is to be compared with its maximum possible value *viz.* $\tilde{\epsilon}_{max} = 0.208$ (for $q = 1$) computed by Mack (1962) ($\tilde{\epsilon} \equiv k_1 A_{11}$ in the notation by Mack (1962)). In figure 11, we plot the shape of the interface at various orders in $\tilde{\epsilon}$. The first-order approximation (leading-order term in $T_1(r; \tilde{\epsilon})$) is $\eta(r, \tilde{t}; \tilde{\epsilon}) = \tilde{\epsilon}\mathrm{J}_0(k_1 r)\cos(2\pi\tilde{t})$ and represents the so-called 'free wave', as the wavenumber k_1 and frequency ω satisfy the dispersion relation. However, all other corrections to $\eta(r, \tilde{t}; \tilde{\epsilon})$ in (3.4), including those in $T_1(r)$, represent 'bound components' as these do not satisfy the dispersion relation. In figure 11 comparing the third-order approximation by Mack

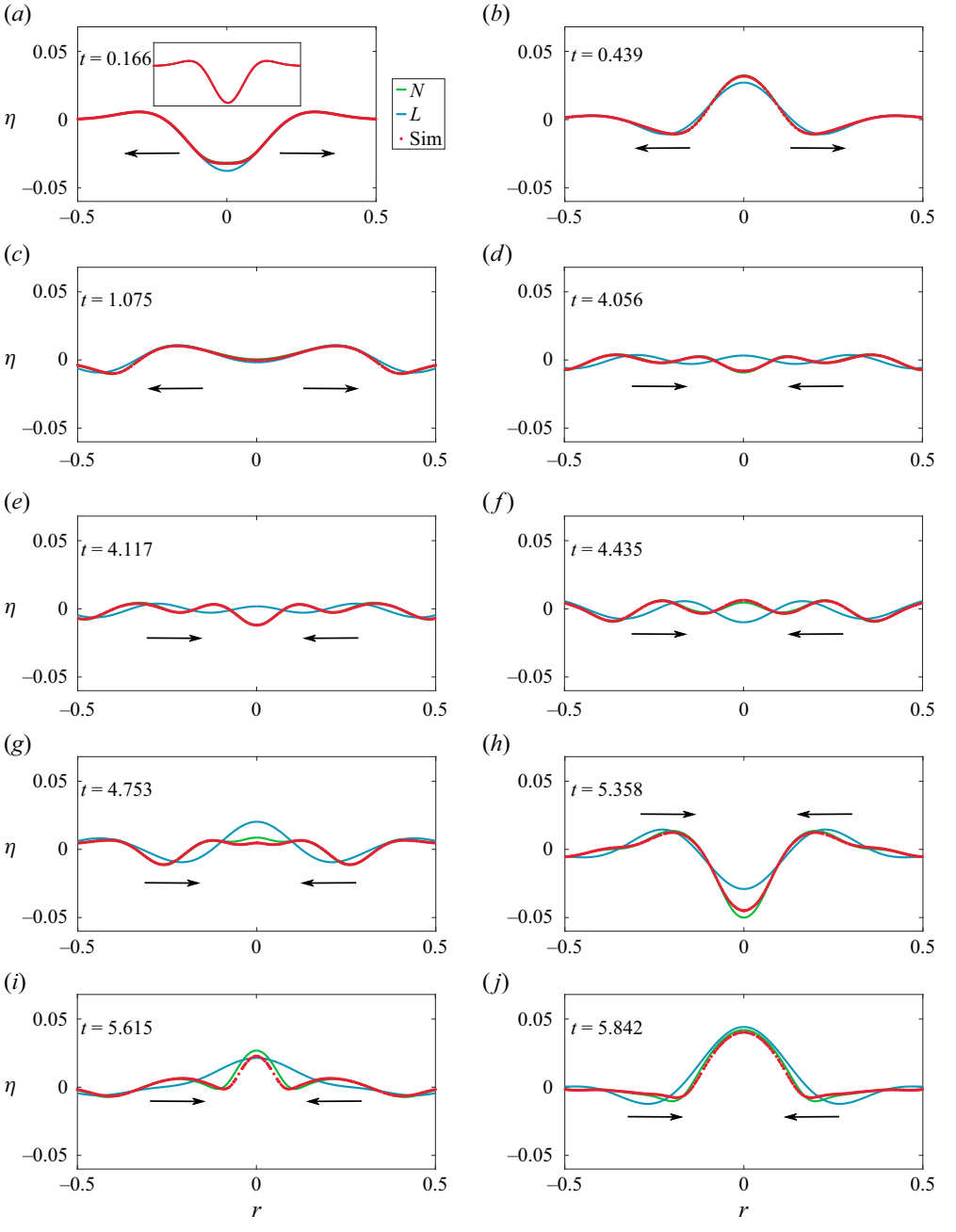

Figure 9. Waves generated from the cavity shaped interface distortion at $t = 0$ (inset of panel (*a*)). We compare the interface shape as a function of time as predicted by linear theory (L, solid blue line), second-order nonlinear theory (N, solid green line) and (inviscid) DNS (Sim, red symbols). The waves reflect off the cylinder wall at $r = 1$ (not shown) and focus back towards $r = 0$ generating oscillations of increasing amplitude. This corresponds to Case 1 of table 1 with $\varepsilon = 0.061$. To highlight the difference between linear and nonlinear predictions, the figures have been plotted up to $r = 0.5$ instead of the entire radial domain up to $r = 1$. The arrows depict the instantaneous direction of motion of the waves. Here (*a*) $t = 0.166$; (*b*) $t = 0.439$; (*c*) $t = 1.075$; (*d*) $t = 4.056$; (*e*) $t = 4.117$; (*f*) $t = 4.435$; (*g*) $t = 4.753$; (*h*) $t = 5.358$; (*i*) $t = 5.615$; (*j*) $t = 5.842$.

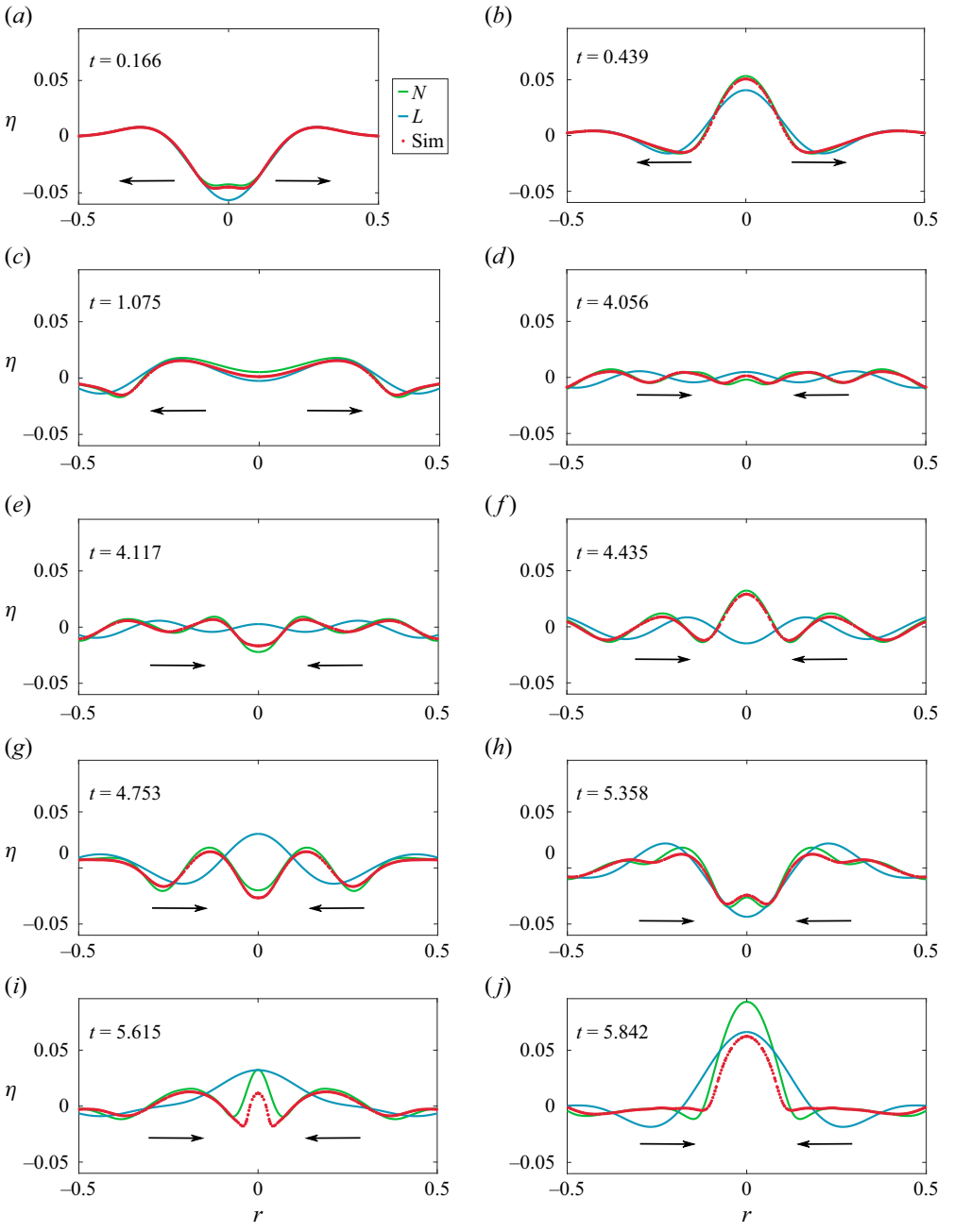

Figure 10. The same as figure 9, but for $\varepsilon = 0.091$ corresponding to Case 2 in table 1. Note the good qualitative agreement between nonlinear theory and (inviscid) DNS but not linear theory, in capturing the dimple in (*h*). Also note the large amplitude oscillations at $r = 0$ with a tendency to generate narrow jet-like structures (*i*, *j*), although no jets are seen. Here (*a*) $t = 0.166$; (*b*) $t = 0.439$; (*c*) $t = 1.075$; (*d*) $t = 4.056$; (*e*) $t = 4.117$; (*f*) $t = 4.435$; (*g*) $t = 4.753$; (*h*) $t = 5.358$; (*i*) $t = 5.165$; (*j*) $t = 5.842$.

(1962) with the numerically computed fourth-order solution, indicates that the former is accurate at this chosen value of $\tilde{\epsilon}$. It is also apparent from figure 11 that the effect of systematically adding bound components (nonlinear contribution) in determining the

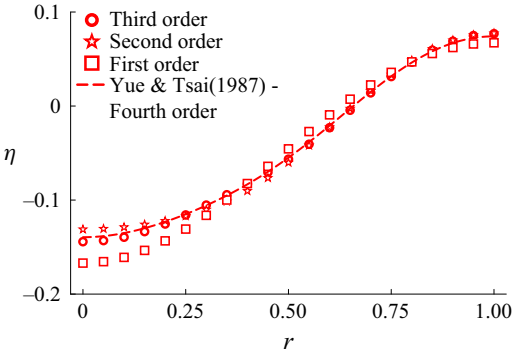

Figure 11. The shape of the interface calculated from (3.4) by retaining terms up to various orders in $\tilde{\epsilon}$ in the expressions for $T_0(r), T_1(r), T_2(r), T_3(r)$. We choose $\tilde{\epsilon} = 0.16703$ and $q = 1$ and plot the interface at $\tilde{t} = 0.5$ when the velocity field everywhere is zero and the shape around $r = 0$ has a depression. A fourth-order interface shape for the same $\tilde{\epsilon}$ is also presented here, obtained following the numerical procedure given in Tsai & Yue (1987).

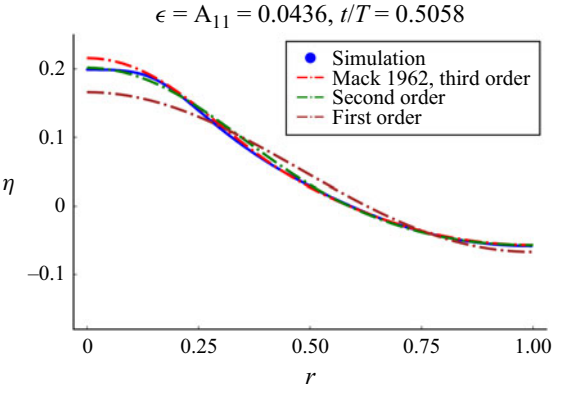

Figure 12. Interface of various orders for $q = 1$ and $\tilde{\epsilon} = 0.16703$. The first, second and third-order solutions are plotted at $\tilde{t} = 1$ using (3.4) of Mack (1962). The numerical solution (indicated in blue as 'simulation') is initialised using the third-order solution of Mack (1962) evaluated at $\tilde{t} = 0.5$. Note that $\tilde{t} = 0.5$ in (3.4) is used to initialise the DNS and hence corresponds to $t = 0$ for the latter.

interface shape, has the largest effect at $r = 0$. This is further established in figure 12. In this figure, the third-order interface depicted in figure 11 ($\tilde{t} = 0.5$) is provided as an initial condition to the simulation. Half a time-period later ($\tilde{t} = 1$), we see that the analytical approximations (i.e. the formulae in Mack (1962)) and the numerical simulation produce a higher elevation at $r = 0$, compared with the first-order approximation (free wave). We particularly highlight the asymmetry at $r = 0$ between the elevation and depressions for the higher-order approximations. For example, the third-order interface and the numerical simulation commence from a depression at $r = 0$ in figure 11, which is visibly less than that for the first-order solution. At $\tilde{t} = 1$ in figure 12, the elevation at $r = 0$ is now significantly more for the solutions which include bound components compared with the free-wave (the first-order solution). This behaviour, typical of nonlinear oscillators, should be contrasted against that of the free wave (a linear oscillator) which generates an elevation at $\tilde{t} = 1$ of the same magnitude as the depression at $\tilde{t} = 0.5$.

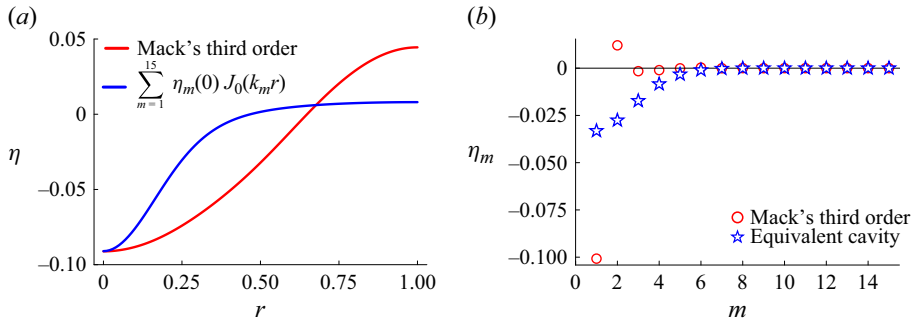

Figure 13. (*a*) A localised cavity shaped deformation (blue) plotted against the delocalised third-order, time-periodic solution (red) by Mack (1962) plotted at a time when it is shaped as a depression around $r = 0$. The Fourier–Bessel series for both shapes are $\eta_m(0)\mathrm{J}_0(k_m r)$ where η_m are provided in (*b*). For the time-periodic solution, $\tilde{\epsilon} = 0.1014$ (third order). The two profiles have been depth matched at $r = 0$. The cavity shape profile has the same dominant Bessel function (k_1) as the free wave in the third-order time periodic solution from (3.4) (Mack 1962). Unlike the cavity, the time-periodic solution is spatially delocalised as it has significant interface displacement at $r = 1$, see (*a*). (*b*) The deformations in (*a*) are expressed as Fourier–Bessel series with coefficients η_m presented in (*b*). The colour scheme is the same in (*a*,*b*). Here (*a*) is the initial interface shape; (*b*) η_m for the cavity ($t = 0$) and for (3.4).

In order to facilitate comparison of the localised initial deformation of current interest, against the time-periodic solution by Mack (1962), it is useful to express (3.4) as a linear superposition over Bessel functions. For this, we need to express the $T_i(r)$, $i = 0, 1, 2, 3$ as a Fourier–Bessel series. Note that for a time-periodic solution, $\eta_m(t; \tilde{\epsilon})$ in (3.5) are also time-periodic and hence may be expressed as Fourier series, i.e.

$$\eta(r, \tilde{t}; \tilde{\epsilon}) = \sum_{m=1}^{N} \eta_m(\tilde{t}; \tilde{\epsilon})\mathrm{J}_0(k_m r) = \sum_{m=1}^{N} \left(\sum_{j=0}^{3} C_m^{(j)}(\tilde{\epsilon}) \cos(2\pi j \tilde{t}) \right) \mathrm{J}_0(k_m r)$$
$$= \sum_{j=0}^{3} \left(\sum_{m=1}^{N} C_m^{(j)}(\tilde{\epsilon})\mathrm{J}_0(k_m r) \right) \cos(2\pi j \tilde{t}) \equiv \sum_{j=0}^{3} T_j(r; \tilde{\epsilon}) \cos(2\pi j \tilde{t}) \qquad (3.5)$$

where $\eta_m(\tilde{t}; \tilde{\epsilon}) \equiv C_m^{(j)}(\tilde{\epsilon}) \cos(2\pi j \tilde{t})$ and the $C_m^{(j)}$ are determined from orthogonality conditions by expressing the $T_j(r)$ in Fourier–Bessel series. Figure 13(*a*) and 13(*b*) present a comparison of the coefficients η_m for Mack (1962) versus η_m for a localised cavity. It is seen that the initial cavity shape whose time evolution has been studied here, have η_m which are significantly different, especially for the lowest wavenumbers. Notably, for the time-periodic solution the η_m change sign, whereas they are all negative for the cavity. In figure 14, we compare the time evolution of the profiles in figure 13(*a*), provided as initial conditions. We refer the reader to the caption of this figure for analogous conclusions about the importance of nonlinearity at $r = 0$.

3.3.2. *Comparison with Basak et al. (2021)*

In this subsection, we explain the apparent significance of nonlinearity around the symmetry axis. To do this, we revisit results for the single Bessel function interface distortion described by $\eta(r, 0) = \varepsilon \mathrm{J}_0(k_5 r)$ (where $\varepsilon > 0$ corresponds to an initial crest at $r = 0$ and $q = 5$ is the wavenumber excited at $t = 0$), as studied in Basak *et al.* (2021). For this initial condition, the expression for $\eta(r, t)$ was analytically derived up to $O(\varepsilon^2)$ in

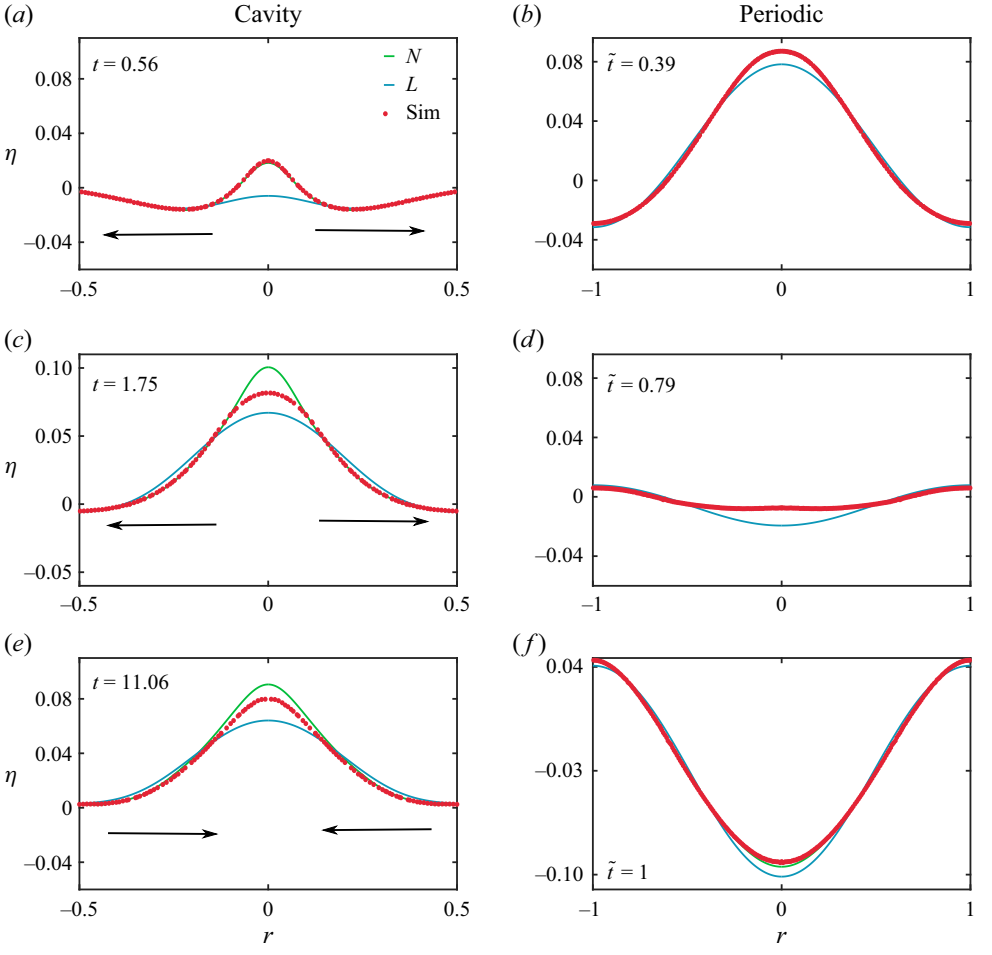

Figure 14. Time evolution starting from the two deformations (and zero velocity in the liquid) shown in figure 13(*a*). Panels (*a*,*c*,*e*) show snapshots of evolution of the cavity at $t = 0.56, 1.75, 11.06$ from numerical simulations (Sim), nonlinear theory (N) obtained from the numerical solution to (2.6) and linear theory. In all cases, the nonlinear theory does significantly better than linear theory. The inward- and outward-propagating arrows show the instantaneous direction of wave propagation. Panels (*b*,*d*,*f*) are the time evolution of the third-order interface shape depicted in figure 13(*a*) (time-periodic solution) at $\tilde{t} = 0.39, 0.79$ and 1.0. One notes the excellent agreement between nonlinear theory and simulations while the difference at $r = 0$ between the linear and nonlinear predictions are maintained. The colour scheme is identical for both columns. Note that air–water surface tension has been used for the simulations. To stay consistent with Mack (1962) where there is no surface tension, we have considered a much larger cylindrical domain here compared with the earlier case. For the simulations, we have used (CGS units) $T = 80$, $g = 981$, $\hat{R}_0 = 100$, $\nu = 0$ (both fluids) with air–water density ratio.

Basak *et al.* (2021) as

$$\eta(r,t) = \underbrace{\varepsilon \mathrm{J}_0(k_5\, r)\cos(\omega_5 t)}_{\text{Primary wave}} + \varepsilon^2 \sum_{j=1}^{\infty} \left[\underbrace{\zeta_1^{(j)}\cos(\omega_j t)}_{\text{Free waves}} + \overbrace{\zeta_2^{(j)}\cos(2\omega_5 t) + \zeta_3^{(j)}}^{\text{Bound waves}} \right] \mathrm{J}_0(k_j r), \tag{3.6}$$

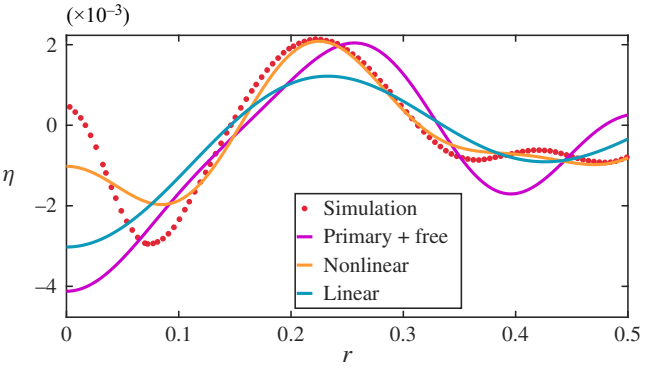

Figure 15. Various approximations for describing the dimple produced from a single Bessel function initial perturbation with moderately large amplitude.

where $\zeta_1^{(j)} + \zeta_2^{(j)} + \zeta_3^{(j)} = 0, \forall j \in \mathbb{Z}^+$ to ensure that the initial condition is satisfied. Note that that (3.6) has been suitably modified from Basak *et al.* (2021) to make this compatible with the length and time scales in the present analysis. Here $\varepsilon = \hat{a}_0/\hat{R}$, frequency $\omega_j = \sqrt{k_j(1+\alpha k_j^2)}$ and expressions for $\zeta_1^{(j)}$, $\zeta_2^{(j)}$ and $\zeta_3^{(j)}$ are provided in the appendix of Basak *et al.* (2021).

As highlighted in (3.6), the expression for $\eta(r,t)$ comprises of three qualitatively different parts. The first term on the right-hand side of (3.6) represents the primary wavenumber which is excited at $t = 0$. This has wavenumber k_5 and oscillates harmonically with frequency ω_5. For ϵ sufficiently large, the initial condition $\eta = \epsilon \mathrm{J}_0(k_5 r)$ represents an interface distortion which is significantly different in shape from that of the corresponding time-periodic solution by Mack (1962) having its free wave as k_5. Due to this mismatch in initial shape, other 'free waves' are generated at $t > 0$ in (3.6) and their frequency satisfy the dispersion relation, i.e. Bessel functions with wavenumber k_j have frequency ω_j. Another kind of waves *viz.* the 'bound waves' also appear at $O(\varepsilon^2)$ and these do not satisfy the dispersion relation. These are necessary to cancel out the contribution from the free waves at $t = 0$. Note that the amplitudes of the free waves *viz.* $\epsilon^2 \zeta_1^{(j)}$ in (3.6), do not evolve in time unlike that in the recent study on triadic resonant interactions among surface waves in Durey & Milewski (2023); see the multiple scale analysis around their equation (4.1). An important difference between this initial condition (Basak *et al.* 2021) and the third-order solution by Mack (1962) is that for the latter, there is only one free component and the rest are all bound components at all t whereas in the former, infinite free and bound components are generated at $t > 0$.

In figure 15, the interface from inviscid DNS with the initial condition $\eta(r,0) = \varepsilon \mathrm{J}_0(k_5 r)$, $\varepsilon = 0.03 > 0$ is shown at an instant when it forms a dimple-like protrusion at $r = 0$. This is represented by the curve with red dots, labelled as 'simulation'. In the same figure, we also plot the formula from Basak *et al.* (2021), excluding the bound components (labelled as 'primary + free'), i.e. setting $\zeta_2^{(j)} = \zeta_3^{(j)} = 0$ in (3.6). It is evident that this approximation does not capture the dimple, which is otherwise predicted by the full nonlinear expression (indicated as 'nonlinear' in the figure caption and referring to (3.6)).

The above exercise can also be carried out when the initial interface deformation takes the shape of a cavity. For this initial condition, $\eta(r,0) = \sum_{m=1}^{\infty} \eta_m(0) \mathrm{J}_0(k_m r)$,

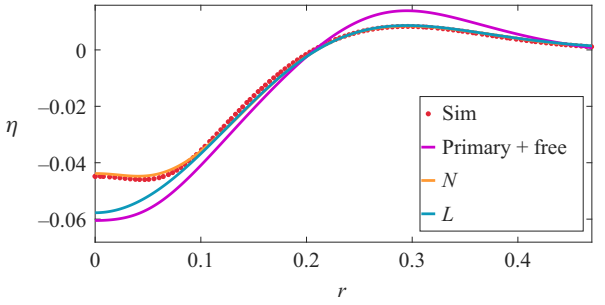

Figure 16. Shape of a dimple for a cavity with $\varepsilon = 0.091$.

as previously shown in figure 5(*a*). From the numerical solution to (2.6), the temporal frequency spectrum at $r = 0$ is obtained. We track the time series generated by $\eta_m(t)$ and eliminate the frequencies $2\omega_m$ and 0 from its Fourier spectrum. Figure 16 demonstrates that after the removal of these bound modes, the interface (labelled 'primary + free') fails to capture the dimple shape. In contrast, the full numerical solution to (2.6) faithfully reproduces the dimple. (We gratefully acknowledge an anonymous referee for several technical clarifications in this section.)

3.4. *Viscous effects: comparison with linear theory*

In this section, we analyse viscous effects for the chosen initial condition. Using cylindrical coordinates, Miles (1968) solved the problem of free-surface waves on a viscous liquid in the linear regime within a radially unbounded domain for a continuous spectrum of wavenumbers in the radial direction. Farsoiya *et al.* (2017) extended this theory to internal waves, considering viscosity and density due to both upper and lower fluids, for a single wavenumber in the initial spectrum. Due to the availability of superposition in the linear regime, the results of Farsoiya *et al.* (2017) are easily extended to initial excitations with multiple wavenumbers. In Cartesian geometry, the single wavenumber initial excitation case was first explicitly studied by Prosperetti (1976) treating free-surface waves and by Prosperetti (1981) treating internal waves. In the Laplace domain and in cylindrical axisymmetric coordinates, the solution to the evolution of a single initial wavenumber k_m was shown in Farsoiya *et al.* (2017) to be given by

$$\tilde{\eta}_m(s) = \hat{\eta}_m(0)\frac{s + \left(4\tilde{k}_m^2\nu - \dfrac{4\tilde{k}_m^3\nu}{\tilde{k}_m + \sqrt{\tilde{k}_m^2 + s/\nu}}\right)}{s^2 + \left(4\tilde{k}_m^2\nu - \dfrac{4\tilde{k}_m^3\nu}{\tilde{k}_m + \sqrt{\tilde{k}_m^2 + s/\nu}}\right)s + \hat{\omega}_m^2}, \qquad (3.7)$$

$$\hat{\omega}_m^2 \equiv g\tilde{k}_m + T\tilde{k}_m^3/\rho, \quad \tilde{k}_m \equiv \frac{k_m}{\hat{R}}.$$

Employing linear superposition, the corresponding (dimensional) expression for the interface evolution in the time domain for the current case becomes

$$\hat{\eta}(\hat{r}, \hat{t}) = \sum_{m=1}^{17} \hat{\eta}_m(\hat{t}) \mathrm{J}_0\left(k_m \frac{\hat{r}}{\hat{R}}\right), \quad \hat{\eta}_m(\hat{t}) \equiv \mathcal{L}^{-1}\left[\tilde{\eta}_m(s)\right]. \qquad (3.8)$$

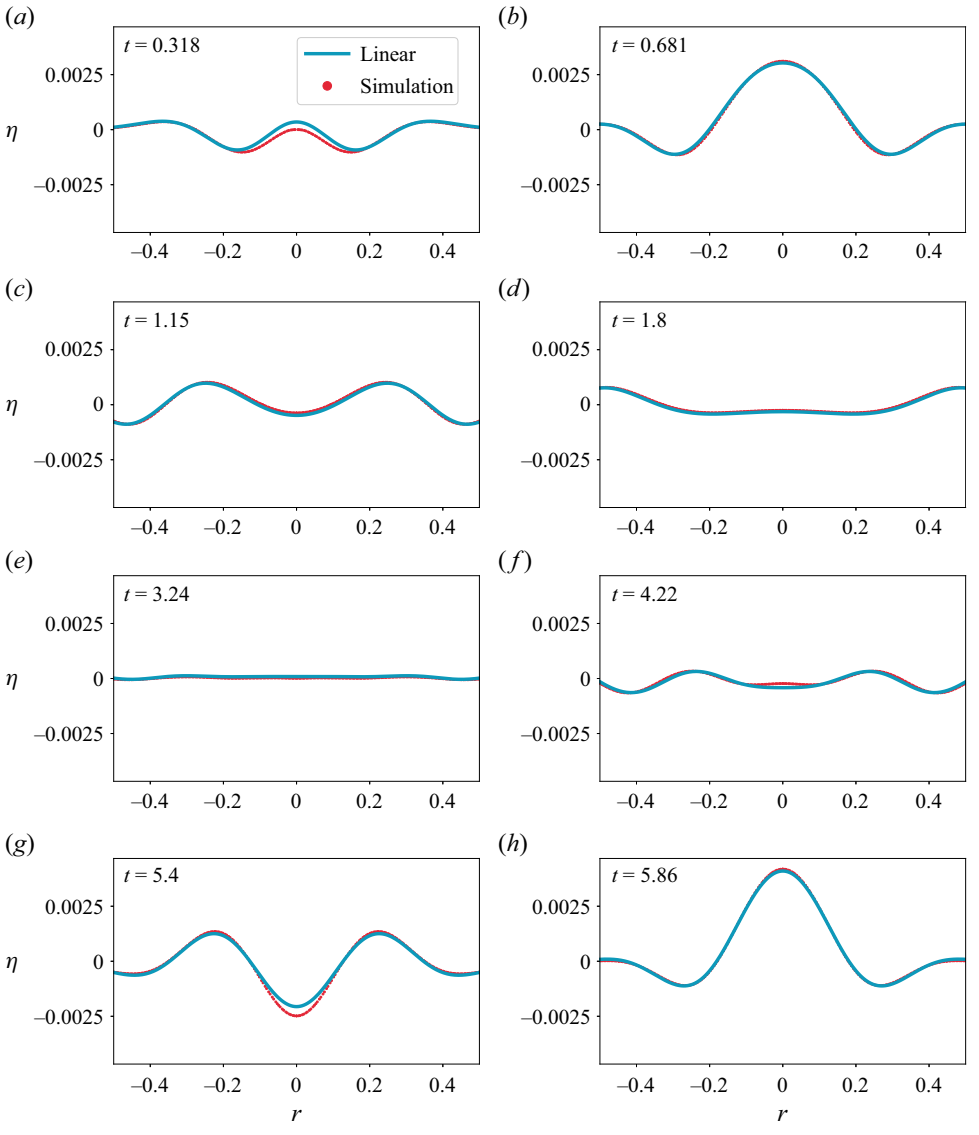

Figure 17. Viscous DNS (indicated as 'simulation' with red dots in the legend to panel (*a*)) with $\varepsilon = 0.006$ and $Oh = 1.17 \times 10^{-3}$ corresponding to Case 10 in table 1. One notes the excellent agreement with linear, viscous theory (blue line, 'linear', (3.8) in text) with hardly any nonlinear contribution.

Here $\mathcal{L}^{-1}$ is the inverse Laplace operator. We stress that (3.7) accounts for dissipation in the bulk liquid and boundary layer, as demonstrated by Prosperetti (1976) in Cartesian coordinates and by Farsoiya *et al.* (2017) in cylindrical coordinates. Equation (3.8) is compared with DNS for two different values of ε and Oh in figures 17 and 18, where inverse Laplace transforms were performed using the Cohen method by Henri Cohen & Zagier (2000) which is a default method in mpmath (2023), a free Python library for arbitrary-precision floating-point arithmetic; see Kayal (2024) for the code. Figure 17 benchmarks the theory at a relatively small $\varepsilon = 0.006$, where linear viscous theory is expected to be accurate. Excellent agreement with linear viscous theory is observed in

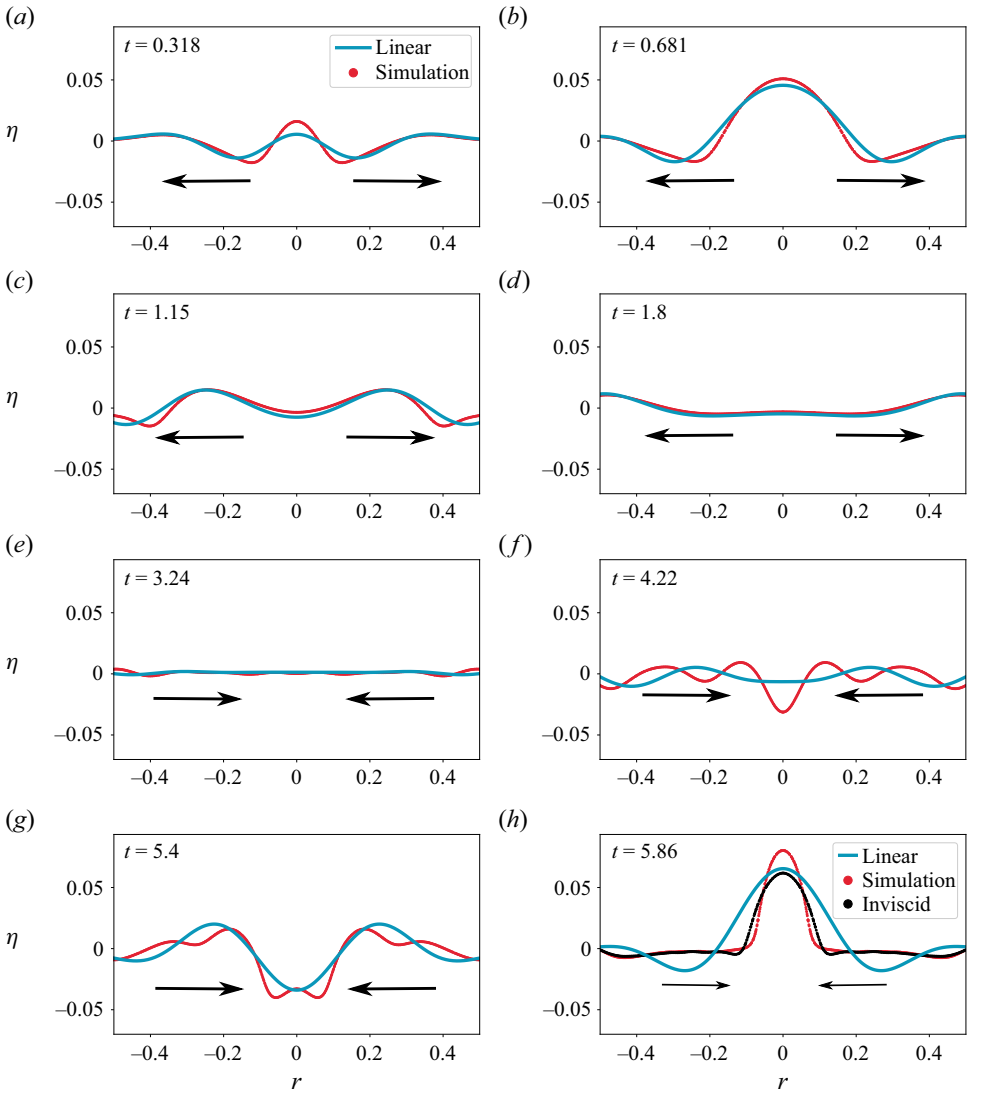

Figure 18. Viscous DNS (indicated as 'simulation' with red dots in the legend to panel (*a*)) with $\varepsilon = 0.091$ and $Oh = 1.17 \times 10^{-4}$ corresponding to Case 4 in table 1. In contrast to figure 17, increasing the value of ε and a corresponding reduction in viscosity, has a dramatic effect in the simulations. We note that viscous linear theory is no longer adequate particularly during the focussing process in (*f–h*). In (*h*), we also provide a comparison of the interface at this time instant, for the inviscid numerical simulation ($Oh = 0$) with the same ε. It is seen that the viscous simulation has a crest which at the indicated instant of time, is taller than the one obtained from the inviscid simulation.

figure 17. Conversely, figure 18 shows a clear distinction between linear and nonlinear predictions.

To further investigate the impact of viscosity, figure 19(*a*) presents the interfacial velocity at $r = 0$ from DNS for various Oh values while figure 19(*b*) represents the interface displacement at $r = 0$, in the same time window. The most notable observation is that the peak velocity at $r = 0$ during wave focussing occurs in the viscous simulation rather than the inviscid one. This non-monotonic behaviour as a function

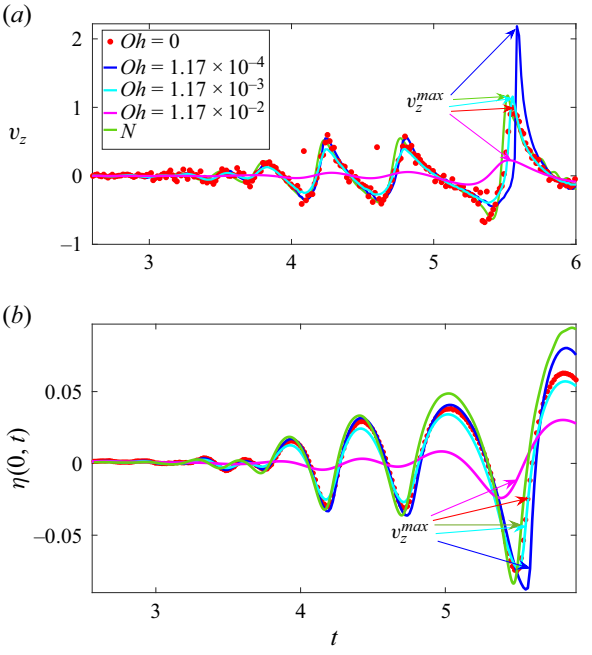

Figure 19. (*a*) Velocity at the interface at $\hat{r} = 0$ for different values of Oh and fixed $\varepsilon = 0.091$. Note that the viscous DNS for $Oh = 1.17 \times 10^{-4}$ (solid deep blue line) produces the largest velocity peak around $t \approx 5.7$. Note in particular that the inviscid signal ($Oh = 0$, red symbols) has a peak which is shorter by a factor of half. This difference is because in the $Oh = 0$ case, we are not resolving the numerically generated boundary layer at the current grid resolution. As discussed in the text, this introduces a degree of grid dependency in the inviscid simulations which cannot be resolved in the numerical framework of the open-source code Basilisk (Popinet & Collaborators 2013–2024). However, for $Oh \geq 1.17 \times 10^{-4}$, we are resolving the boundary layers and the results are grid convergent. (*b*) The interface height $\eta(0, t)$ with the same colour scheme as in (*a*). We refer the reader to Appendix C where the grid convergence results for this (and other) simulations are provided.

of the Ohnesorge number is a well-known phenomenon in other contexts (Duchemin *et al.* 2002; Ghabache *et al.* 2014*a*), indicating a significant effect of viscosity. In our analysis of converging waves, we attribute the observed non-monotonic behaviour to viscous dissipation within the boundary layer at the gas–liquid interface. Even as the Ohnesorge number approaches zero ($Oh = 0^+$), this boundary layer remains significant, similar to the dissipative anomaly seen in fully developed turbulence (Prandtl 1904; Onsager 1949; Eggers 2018; Dubrulle 2019) and recently explored in contexts such as sheet retraction (Sanjay *et al.* 2022) and drop impact (Sanjay, Chantelot & Lohse 2023; Sanjay & Lohse 2024) interfacial flows. Consequently, this non-zero viscous dissipation intensifies the focussing of capillary waves, thereby increasing the velocity at the centre ($r = 0$). To validate this hypothesis, in the next section, we next employ the viscous potential flow approach, which accounts for bulk viscous dissipation but neglects dissipation in the gas–liquid boundary layer, to model the converging waves.

We emphasise that DNS for $Oh < 1.17 \times 10^{-4}$ exhibit grid dependency, as indicated by the pink shaded region in figure 21(*a*,*b*). This dependency arises from insufficient grid resolution to properly resolve the boundary layer in low-viscosity liquids, a challenge analogous to those encountered in wall-bounded turbulence studies (Lohse & Shishkina 2024) and classical contact line simulations (Snoeijer & Andreotti 2013). These fields

continue to grapple with resolving multiple scales spanning orders of magnitude. We designate this unresolved region in pink, highlighting an open problem for future multiscale simulations. The $Oh = 0$ simulation, represented by symbols in figure 19(a), demonstrates grid dependency in velocity at $r = 0$ for resolutions up to 2048^2 (maximum adaptive level). This manifests as isolated 'spike' points in figure 24(a). In contrast, the nonlinear analytical prediction, depicted by the green curve labelled 'N' in figure 19(a), does not exhibit such spikes. In the (inviscid) Euler limit, our results align with inviscid nonlinear theory (see figures 9 and 10). However, we stress that this scenario also exhibits grid dependency. The one-fluid approximation used in Basilisk to solve Euler equations creates an over-constrained system by enforcing continuity of tangential velocity at the gas–liquid interface, which is incompatible with Euler equations. Consequently, indefinite grid refinement generates deviations, as evident in figure 24(a). Lastly, despite setting $Oh = 0$, our simulations retain a non-zero, grid-dependent viscosity. These factors should be considered when interpreting comparisons between inviscid, potential flow theory (where tangential velocity at the interface is discontinuous) and our numerical results obtained from Basilisk.

3.5. *Viscous potential flow*

To further elucidate viscous effects, we incorporate viscosity into the nonlinear equations using the viscous potential flow (VPF) model (Joseph 2006). Unlike the linear case discussed previously, this method does not account for the boundary layer formed at the free surface, since it does not enforce the zero shear stress boundary condition (Moore 1963). As is well known, in this approach the normal stress boundary condition (2.1c) is modified to incorporate the effect of bulk viscous damping to obtain

$$\left(\frac{\partial\phi}{\partial t}\right)_{z=\eta} + \eta + 2\,b\,Oh\,\sqrt{\alpha}\,\left(\frac{\partial^2\phi}{\partial z^2}\right)_{z=\eta} + \frac{1}{2}\left\{\left(\frac{\partial\phi}{\partial r}\right)^2 + \left(\frac{\partial\phi}{\partial z}\right)^2\right\}_{z=\eta} - \alpha\left(\frac{\partial^2\eta}{\partial r^2} + \frac{1}{r}\frac{\partial\eta}{\partial r}\right) = 0. \tag{3.9}$$

We follow the same strategy as the inviscid case and obtain a modified differential equation for η_n, i.e. the viscous counterpart of (2.6) leading to

$$\begin{aligned}&\frac{\mathrm{d}^2\eta_n}{\mathrm{d}t^2} + \omega_n^2\eta_n + 2\,b\,Oh\,\sqrt{\alpha}\,k_n^2\frac{\mathrm{d}\eta_n}{\mathrm{d}t} + 2b\,Oh\,\sqrt{\alpha}\,k_n\sum_{m,p}k_m^2 C_{npm}\frac{\mathrm{d}\eta_m}{\mathrm{d}t}\eta_p \\ &\quad + k_n\sum_{m,p}\left[1 + \frac{k_p^2 - k_m^2 - k_n^2}{2k_mk_n}\right]C_{npm}\left(\frac{\mathrm{d}^2\eta_m}{\mathrm{d}t^2}\right)\eta_p \\ &\quad + \frac{1}{2}k_n\sum_{m,p}\left[1 + \frac{k_p^2 + k_m^2 - k_n^2}{2k_mk_p} + \frac{k_p^2 - k_m^2 - k_n^2}{k_mk_n}\right]C_{npm}\left(\frac{\mathrm{d}\eta_m}{\mathrm{d}t}\right)\left(\frac{\mathrm{d}\eta_p}{\mathrm{d}t}\right) = 0.\end{aligned} \tag{3.10}$$

In figure 20, we compare the nonlinear analytical inviscid solution (referred to as 'inviscid' in the legend), the VPF solution for $\varepsilon = 0.091$ and the viscous DNS (referred to as 'simulation') for Case 4 in table 1. It is seen that the VPF solution, is indistinguishable

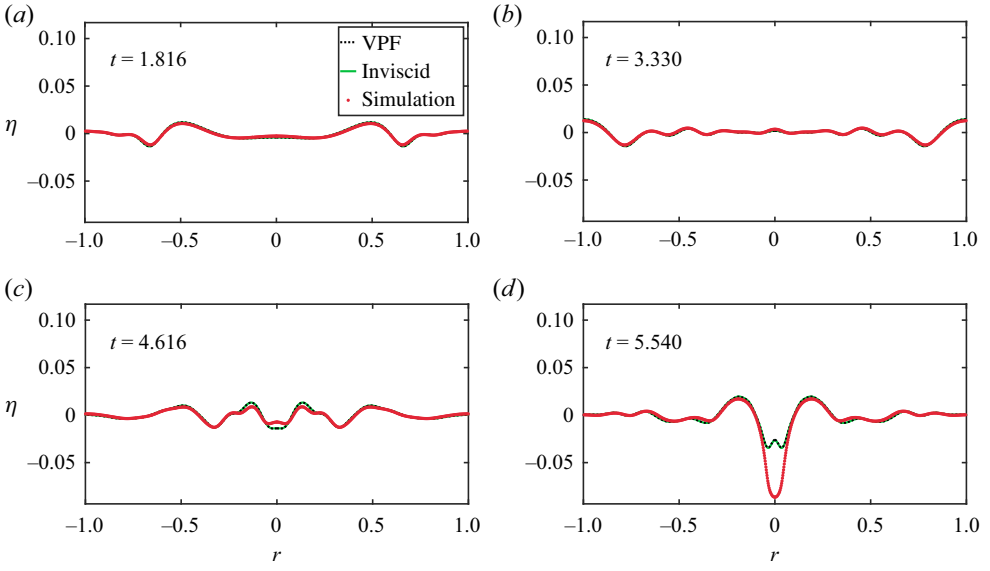

Figure 20. Comparison of the VPF (black dotted line), inviscid solution (green solid line) and DNS (red dots) at $\varepsilon = 0.091$ and $Oh = 1.17 \times 10^{-4}$, Case 4 in table 1.

from the inviscid one in the limit of $Oh = 0^+$, highlighting the importance of resolving the viscous boundary layer in theory.

To further quantify the comparison between these cases, in figure 21(a) shows the maximum velocity at the axis of symmetry within a shallow cavity during focussing. The linear viscous theory, which accounts for the boundary layer at the free surface, describes the change in v_z with Ohnesorge number slightly better than the VPF model. Figure 21(b) presents results for a deeper cavity where nonlinearity plays a significant role, and the non-monotonic behaviour observed in figure 19(a) as a function of Oh is evident. The VPF model fails to capture this non-monotonic behaviour, highlighting the importance of resolving the boundary layer at the gas–liquid interface, as discussed in § 3.4. We propose developing a nonlinear-viscous theory superior to the VPF model to explain the observations in figures 19 and 21(b) in future work.

4. Conclusion and outlook

In this study, we have discussed the dynamics of a localised free-surface perturbation in a cylindrical pool of liquid, which generates a train of waves. These waves, upon reflecting from the container walls, converge back towards the axis of symmetry, leading to progressively increasing free-surface oscillations at the centre. Using the potential flow approximation, we derived a set of ODEs governing the evolution of amplitudes up to second order.

For shallow cavities, linear theory suffices to explain the wave evolution. However, as the cavity depth increases, the limitations of linear theory become evident, particularly in predicting the focussing effects at $r = 0$. Our findings demonstrate that linear dispersive focussing alone is inadequate to describe the intricate dimple shape forming at the axis of symmetry for deeper cavities. A nonlinear theory that accounts for the generation of

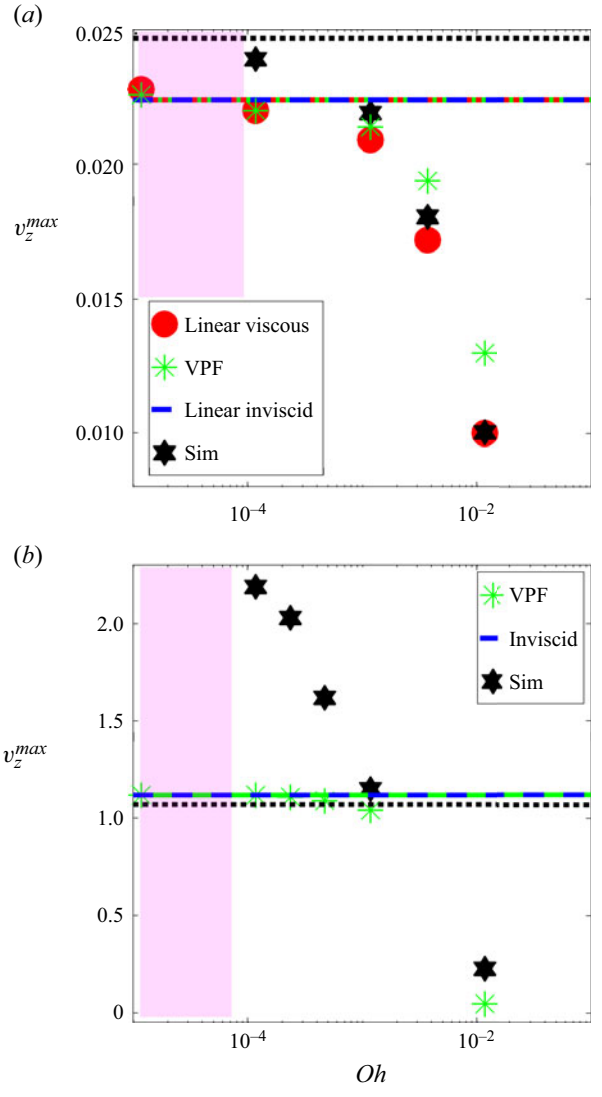

Figure 21. Comparison of the maximum velocity at $r = 0$, i.e. v_z^{max} (see arrows in figure 19*a*) after reflection for different Ohnesorge number for a shallow cavity, Cases 7, 9, 10, 11, 12 in table 1 (panel (*a*)) and for a deep cavity, Cases 2, 4, 5, 6, 13, 14 (panel (*b*)). In (*a*) the '+' symbols represent DNS with finite viscosity. Black dotted line represents DNS with zero viscosity. Red symbols represent the linear viscous solution obtained by numerical inversion of (3.7). Green symbols indicate VPF approximation obtained from solving (3.10). At the $Oh = 0$ limit, VPF (green dashed line) and linear viscous theory (red dashed line) coincide with the linear inviscid theory (blue dashed line). In panel (*b*) the symbols have the same meaning as in (*a*), the only difference is that we have employed nonlinear inviscid theory (blue dashed line) in this case. Note that non-monotonicity in the velocity at $r = 0$ as a function of Oh. The VPF approximation despite being nonlinear is unable to describe this non-monotonicity, presumably because of its inability to resolve the boundary layer at the free surface. The dotted black line represents the velocity of inviscid DNS which shows grid dependency. In the current figure, below a certain value of Oh (pink shaded region) grid dependency persists in our simulations, due to the presence of an unresolved thin boundary layer. We do not depict this data here due to the lack of this convergence. For $Oh > 1.17 \times 10^{-4}$, however, the boundary layers are resolved for simulation points '+' and the data are grid converged. Note that the nonlinear inviscid theory ($Oh = 0$, dashed blue line) predicts $v_z^{max}(r = 0)$ which is smaller than the prediction by DNS for $Oh \approx 1.17 \times 10^{-4}$ by a factor ≈ 2. A similar albeit significantly more intensification at an optimal value of Oh was first noted in the case of bubble bursting in the seminal study by Duchemin *et al.* (2002); see their figure 12. Here (*a*) shallow cavity with $\varepsilon = 0.006$; (*b*) deep cavity with $\varepsilon = 0.091$.

bound components is found to be essential for accurately modelling the focussing process. The role of bound components is particularly critical in capturing the interface evolution at the symmetry axis.

A notable observation is the significant influence of viscosity on the focussing process. Interestingly, the maximum velocity at the axis of symmetry is higher for a slightly viscous fluid than for an inviscid one. This non-monotonic behaviour with respect to the Ohnesorge number Oh is not captured by either the linear viscous model (Prosperetti 1976; Farsoiya *et al.* 2017) or the nonlinear VPF model (Joseph 2006). The VPF model's failure, stemming from its neglect of boundary layer effects, underscores the critical role of these layers in the $Oh \to 0^+$ limit. As the VPF model converges to an inviscid solution in this limit, it further emphasises the boundary layers' importance in velocity enhancement. The singular nature of the $Oh \to 0^+$ limit arises from fundamental disparities between Navier–Stokes and Euler equations. Even as Oh approaches zero, the no-slip condition at the liquid–gas interface necessitates a boundary layer, preserving viscous effects.

In conclusion, we emphasise some interesting observations and hypothesis made in Zhang & Thoroddsen (2008) concerning capillary wave focussing, albeit on a spherical bubble unlike the flat surface treated here. Some of these find qualitative support from our theory. In page 9, first column, first paragraph of Zhang & Thoroddsen (2008), the authors remark insightfully that the wave convergence process is itself not necessarily nonlinear, as the large amplitude oscillations seen in their figure 14 are also predicted by linear theory. However, linear amplification itself may not be enough to trigger pinch-off, emphasising the local importance of nonlinearity at the focal point. Our analysis establishes that this is qualitatively true, cf. figure 18. In their section C (p. 9), Zhang & Thoroddsen (2008) also emphasise that the phase and amplitude of the wavetrain is very important to the convergence process. Our nonlinear analysis establishes the importance of the amplitude of the wavetrain while the viscous analysis demonstrates that the VPF model (which does not resolve the interface boundary layer) is unable to capture the non-monotonic dependence of vertical velocity at $r = 0$ on Oh. Presumably, this non-monotonicity will be predicted from a nonlinear, viscous model, which is still simpler than the full Navier–Stokes equation and this is proposed as future work. Upcoming research thus needs to develop a comprehensive, nonlinear viscous theory that incorporates boundary layer effects and also accounts for the nonlinearity associated with focussing. Additionally, extending this work to non-Newtonian fluids, such as viscoplastic or viscoelastic liquids (Sanjay, Lohse & Jalaal 2021), could reveal new insights and broaden the applicability of our theoretical framework.

Supplementary material. Supplementary movies are available at https://doi.org/10.1017/jfm.2024.1089. Movie 1, comparison of cavity evolution at $\varepsilon = 0.61$; movie 2, inviscid DNS of cavity evolution at $\varepsilon = 0.91$. All codes are available at Kayal (2024).

Acknowledgements. R.D. thanks Professor B. Sutherland for sharing the study by Smith (1976). V.S. thanks Professor D. Lohse for stimulating discussions on viscous anomaly.

Funding. We gratefully acknowledge financial support from DST-SERB (Government of India) grants MTR/2019/001240, CRG/2020/003707 and SPR/2021/000536 on topics related to waves, jet formation, cavity collapse and the viscous Cauchy–Poisson problem. The PhD tenure of L.K. is supported by the Prime-Minister's Research Fellowship (PMRF), Government of India and is gratefully acknowledged. V.S. acknowledges funding from NWO and Canon under the project FIP-II.

Declaration of interests. The authors report no conflict of interest.

Author ORCIDs.
Vatsal Sanjay https://orcid.org/0000-0002-4293-6099;
Ratul Dasgupta https://orcid.org/0000-0003-0621-3472.

Appendix A

The expressions for the third-order approximation to $\eta(r,\tilde{t};\tilde{\epsilon})$ by Mack (1962) expressed in our notation are

$$T_0(r;\tilde{\epsilon}) \equiv \frac{1}{4}\tilde{\epsilon}^2 k_1(\mathrm{J}_{01}^2 - \mathrm{J}_{11}^2), \tag{A1}$$

$$\begin{aligned} T_1(r;\tilde{\epsilon}) \equiv \tilde{\epsilon}\mathrm{J}_{01} + \frac{\tilde{\epsilon}^3 k_1^2}{4}\Bigg\{ & \mathrm{J}_{01}^3 - \frac{5}{2}\mathrm{J}_{01}\mathrm{J}_{11}^2 \\ & + \frac{\mathrm{J}_{11}^3}{k_1 r} + \frac{1}{8}\sum_{i=1}^{\infty}\frac{k_i\Gamma_i\mathrm{J}_{01}\mathrm{J}_{0i}}{k_1} - \frac{1}{4}\sum_{i=1}^{\infty}\frac{k_i^2\Gamma_i\mathrm{J}_{01}\mathrm{J}_{0i}}{k_1^2} - \sum_{i=1}^{\infty}\frac{1}{8}\frac{k_i^2\Gamma_i\mathrm{J}_{11}\mathrm{J}_{1i}}{k_1^2} \\ & + \frac{1}{4}\sum_{i=1}^{\infty}\frac{k_i\Gamma_i\mathrm{J}_{01}\mathrm{J}_{0i}}{k_1} + \sum_{i=2}^{\infty}\frac{(k_i/k_1)\mathrm{J}_{0i}}{1-(k_i/k_1)}\Bigg[- \alpha_n[\mathrm{J}_{01}^3] - \alpha_n[\mathrm{J}_{01}\mathrm{J}_{11}^2] \\ & + \alpha_n\left[\frac{\mathrm{J}_{11}^3}{k_1 r}\right] - \frac{1}{4}\sum_{j=1}^{\infty}\frac{k_j^2\Gamma_j\alpha_n[\mathrm{J}_{01}\mathrm{J}_{0j}]}{k_1^2} + \frac{1}{2}\sum_{j=1}^{\infty}\frac{k_j\Gamma_j\alpha_n[\mathrm{J}_{01}\mathrm{J}_{0j}]}{k_1} \\ & - \frac{1}{8}\sum_{j=1}^{\infty}\frac{k_j^2\Gamma_j\alpha_n[\mathrm{J}_{11}\mathrm{J}_{1j}]}{k_1^2}\Bigg]\Bigg\}, \end{aligned} \tag{A2}$$

$$T_2(r;\tilde{\epsilon}) \equiv \frac{\tilde{\epsilon}^2 k_1}{4}\left(\mathrm{J}_{01}^2 - \mathrm{J}_{11}^2 - \frac{1}{4}\sum_{i=1}^{\infty}\frac{k_i\Gamma_i\mathrm{J}_{0i}}{k_1}\right), \tag{A3}$$

$$\begin{aligned} T_3(r;\tilde{\epsilon}) \equiv \frac{\tilde{\epsilon}^3 k_1^2}{12}\Bigg(& \mathrm{J}_{01}^3 - \frac{7}{2}\mathrm{J}_{01}\mathrm{J}_{11}^2 + \frac{\mathrm{J}_{11}^3}{k_1 r} - \frac{1}{8}\sum_{i=1}^{\infty}\frac{k_i\Gamma_i\mathrm{J}_{01}\mathrm{J}_{0i}}{k_1} \\ & - \frac{1}{4}\sum_{i=1}^{\infty}\frac{k_i^2\Gamma_i\mathrm{J}_{01}\mathrm{J}_{0i}}{k_1^2} + \sum_{i=1}^{\infty}\frac{1}{8}\frac{k_i^2\Gamma_i\mathrm{J}_{11}\mathrm{J}_{1i}}{k_1^2} \\ & + \frac{1}{4}\sum_{i=1}^{\infty}\frac{k_i\Gamma_i\mathrm{J}_{01}\mathrm{J}_{0i}}{k_1} - \frac{1}{9}\sum_{i=1}^{\infty}\frac{(k_i/k_1)\mathrm{J}_{0i}}{1-(k_i/9k_1)}\Bigg[5\alpha_n[\mathrm{J}_{01}^3] + \frac{7}{2}\alpha_n[\mathrm{J}_{01}\mathrm{J}_{11}^2] \\ & - \alpha_n\left[\frac{\mathrm{J}_{11}^3}{k_1 r}\right] - \frac{5}{2}\sum_{j=1}^{\infty}\frac{k_j\Gamma_j\alpha_n[\mathrm{J}_{01}\mathrm{J}_{0j}]}{k_1} + \frac{1}{4}\sum_{j=1}^{\infty}\frac{k_j^2\Gamma_j\alpha_n[\mathrm{J}_{01}\mathrm{J}_{0j}]}{k_1^2} \\ & + \frac{1}{8}\sum_{j=1}^{\infty}\frac{k_j^2\Gamma_j\alpha_n[\mathrm{J}_{11}\mathrm{J}_{1j}]}{k_1^2} - \sum_{j=1}^{\infty}\frac{k_j\Gamma_j\alpha_n[\mathrm{J}_{11}\mathrm{J}_{1j}]}{k_1}\Bigg]\Bigg). \end{aligned} \tag{A4}$$

The $O(\tilde{\epsilon}^3)$ accurate, nonlinear frequency $\omega(\tilde{\epsilon}, q = 1)$ is given by

$$\omega^2(\tilde{\epsilon}, q = 1) = k_1 \left\{ 1 + \frac{\tilde{\epsilon}^2 k_1^4}{4} \left(-\alpha_1[\mathrm{J}_{01}^3] - \alpha_1[\mathrm{J}_{01}\mathrm{J}_{11}^2] + \alpha_1 \left[\frac{\mathrm{J}_{11}^3}{k_1 r} \right] - \frac{1}{4} \sum_{i=1}^{\infty} \frac{k_i^2 \Gamma_i \mathrm{J}_{01} \mathrm{J}_{0i}}{k_1^2} \right.\right.$$
$$\left.\left. + \frac{1}{2} \sum_{i=1}^{\infty} \frac{k_i \Gamma_i \alpha_1[\mathrm{J}_{01}\mathrm{J}_{0i}]}{k_1} - \frac{1}{8} \sum_{i=1}^{\infty} \frac{k_i^2 \Gamma_i \alpha_1[\mathrm{J}_{11}\mathrm{J}_{1i}]}{k_1} \right) \right\} \tag{A5}$$

with the functionals $\alpha[\cdot]$ and $\gamma[\cdot]$ defined as

$$\alpha_n[F(r)] \equiv \frac{\int_0^1 rF(r)\mathrm{J}_{0n}\,\mathrm{d}r}{\frac{1}{2}(\mathrm{J}_0(k_n))^2}, \quad \Gamma_i[F(r)] \equiv \frac{2\alpha_n[\mathrm{J}_{01}^2] + 2\alpha_n[\mathrm{J}_{11}^2]}{1 - \frac{k_n}{4k_1}}. \tag{A6}$$

We have used the definitions $\mathrm{J}_1(k_n) = 0 (n = 1, 2, 3, \ldots)$ and the shorthand notation $\mathrm{J}_{ij} = \mathrm{J}_i(k_j r)$.

Appendix B

We derive the relation between the nonlinear interaction coefficients C_{mnq} and D_{mnq} discussed in (2.5). This relation has been provided in Nayfeh (1987) and Miles (1976) without proof and the same is presented here. Following Nayfeh (1987), we represent (2.1) a in (semi) basis-independent notation as

$$\phi(\boldsymbol{x}, z, t) = \sum_{m=1}^{\infty} \phi_m(t) \Psi_m(\boldsymbol{x}) \exp(k_m z), \tag{B1}$$

where $\boldsymbol{x}$ is the horizontal position vector and Ψ_m satisfies the equation $\nabla_H^2 \Psi_m + k_m^2 \Psi = 0$ as a consequence of ϕ satisfying the Laplace equation; note that $\nabla^2 = \nabla_H^2 + \partial^2/\partial z^2$. We assume that $\Psi_m(\boldsymbol{x})$ follow the orthogonality rule $\iint \mathrm{d}S\ \psi_m(\boldsymbol{x})\psi_q(\boldsymbol{x}) = \delta_{mq} S$ where δ_{mq} is the Kronecker delta. Using Stokes theorem to relate an area integral (over s) in two dimensions to the line integral, we have for a vector field $\boldsymbol{F}(\boldsymbol{x})$

$$\iint \mathrm{d}s\ \nabla_H \cdot \boldsymbol{F} = \int \mathrm{d}l\,(\boldsymbol{F} \cdot \boldsymbol{n})\,. \tag{B2}$$

Choosing $\boldsymbol{F} = \psi_q \psi_m \nabla_H \psi_n$, (B2) leads to

$$\iint \left[\psi_q\,(\nabla_H \psi_m \cdot \nabla_H \psi_n) + \psi_m \left(\nabla_H \psi_q \cdot \nabla_H \psi_n \right) + \psi_q \psi_m \nabla_H^2 \psi_n \right] \mathrm{d}s = 0, \tag{B3}$$

the right-hand side following from the no-penetration condition at the wall. Following the same notation as Nayfeh (1987), we define

$$\iint \mathrm{d}s\ \psi_m(\boldsymbol{x})\psi_n(\boldsymbol{x})\psi_q(\boldsymbol{x}) \equiv S\ C_{mnq}, \quad \iint \mathrm{d}s\ \left(\nabla_H \psi_m(\boldsymbol{x}) \cdot \nabla_H \psi_n(\boldsymbol{x})\right) \psi_q(\boldsymbol{x}) \equiv S\ D_{mnq}. \tag{B4}$$

Note that $D_{nmq} = D_{mnq}$. Using (B4), (B3) may be written compactly as

$$D_{mnq} + D_{qnm} - k_n^2 C_{mnq} = 0. \tag{B5}$$

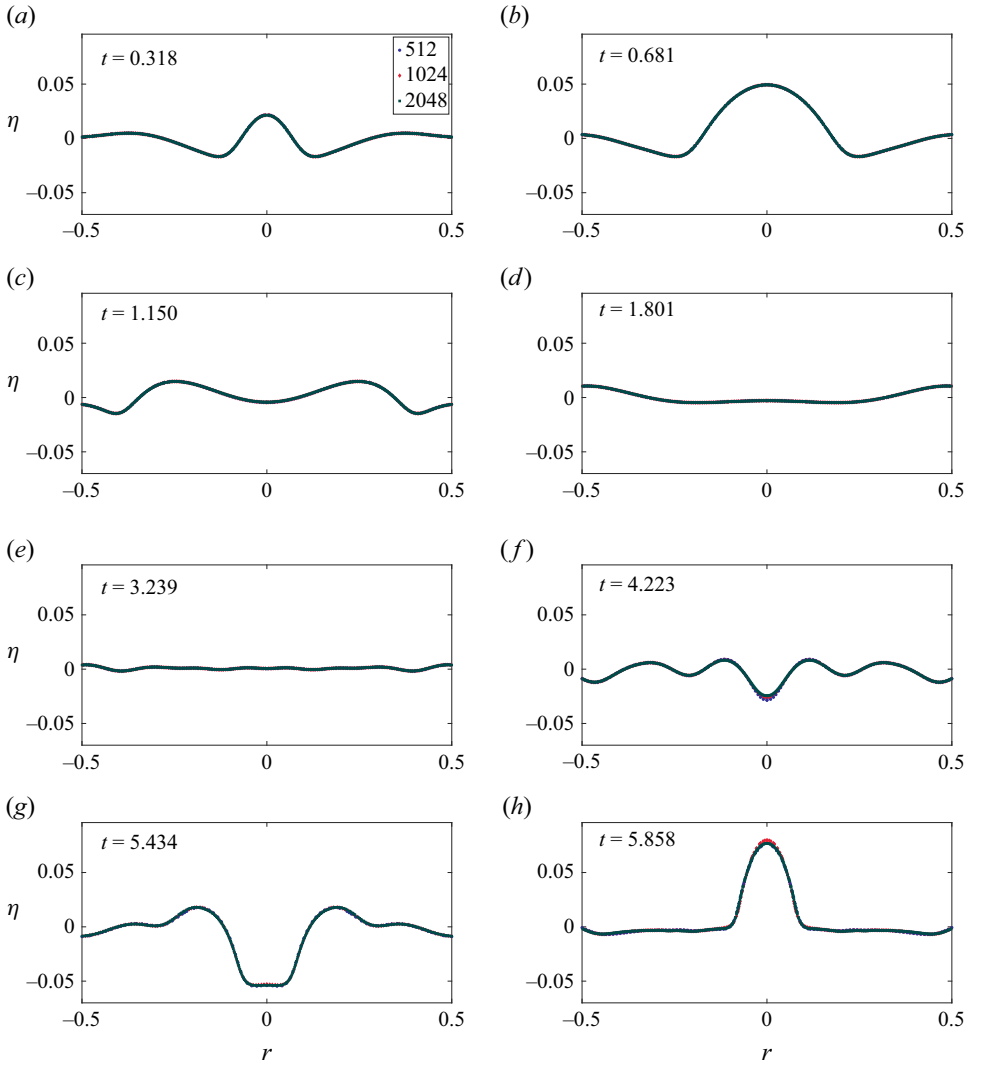

Figure 22. Comparison of interface profile for Case 4 in table 1 at three different grid resolutions, 512^2 (blue dots), 1024^2 (red dots) and 2048^2 (green dots).

Replacing $m \to n, n \to q, q \to m$ in (B5), we obtain

$$D_{nqm} + D_{mqn} - k_q^2 C_{nqm} = 0, \tag{B6}$$

which may be rewritten as

$$D_{qnm} + D_{qmn} - k_q^2 C_{nqm} = 0. \tag{B7}$$

Using (B7) in (B5), we obtain

$$D_{mnq} = k_n^2 C_{mnq} - \left(k_q^2 C_{nqm} - D_{qmn}\right). \tag{B8}$$

Replacing once again $m \to q, n \to m, q \to n$ in (B5), we obtain

$$D_{qmn} + D_{nmq} - k_m^2 C_{qmn} = 0. \tag{B9}$$

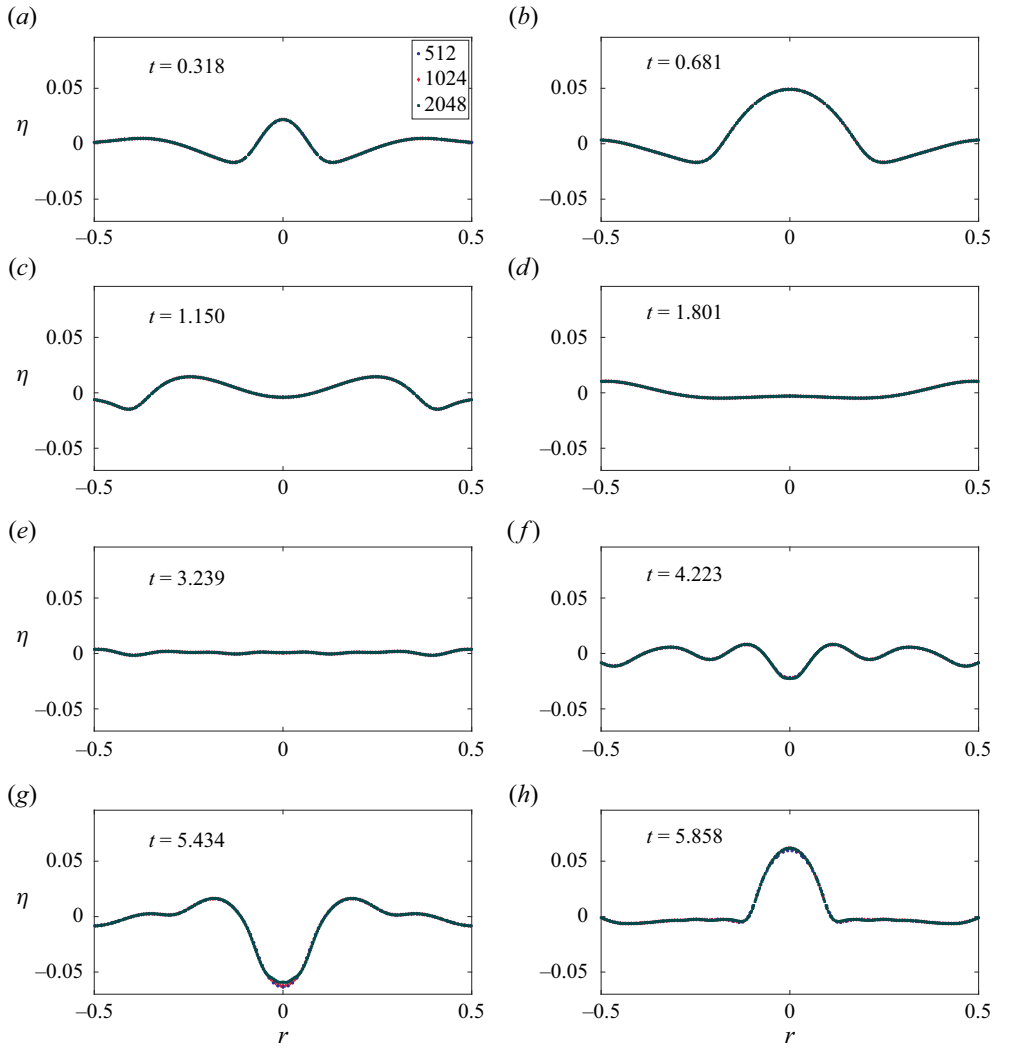

Figure 23. Comparison of interface profile for Case 2 in table 1 for three different grid resolutions, 512^2 (blue dots), 1024^2 (red dots) and 2048^2 (green dots).

Combining (B8) and (B9) and the fact that $D_{mnq} = D_{nmq}$, we obtain

$$D_{nmq} = \frac{1}{2}\left(k_n^2 + k_m^2 - k_q^2\right) C_{nmq}. \tag{B10}$$

After some manipulation, (2.5) follows from the above expression.

Appendix C

Figures 22 and 23 illustrate grid convergence results at three resolutions (512^2, 1024^2 and 2048^2) for Cases 4 and 2, respectively, from table 1. Figure 24(*a*,*b*) present grid convergence for the velocity at the symmetry axis.

For the inviscid case ($Oh = 0$, figure 24*a*), while the overall vertical velocity trend remains consistent, the presence of spikes and the magnitude exhibit grid refinement

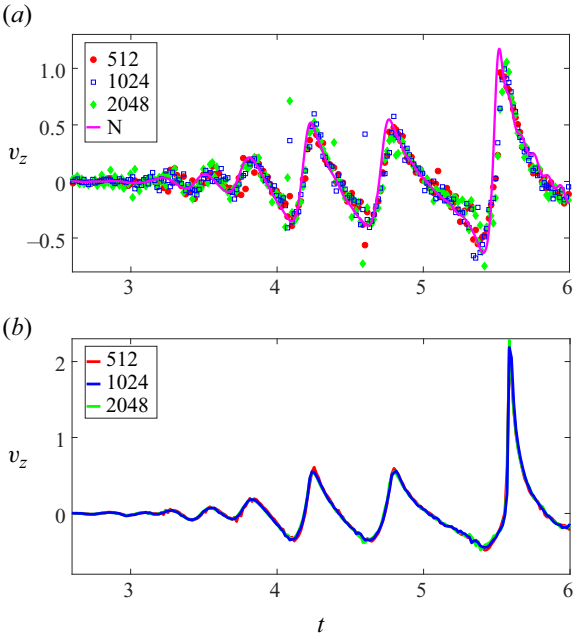

Figure 24. Comparison of the vertical velocity for Case 2 (panel (*a*)) and Case 4 (panel (*b*)) for three different grid resolutions, 512^2 (red solid line), 1024^2 (blue solid line) and 2048^2 (green solid line). In (*a*), we also provide the prediction from the numerical solution to the analytical model from (2.6) indicated as 'N' in the figure. Here (*a*) $Oh = 0$; (*b*) $Oh = 1.17 \times 10^{-4}$.

sensitivity. To provide a robust reference, we include the inviscid, nonlinear analytical solution in figure 24(*a*) denoted by '*N*'. This demonstrates good agreement with the $Oh = 0$, DNS solution, capturing the main temporal velocity variation features without spurious peaks, thus validating the observed simulation behaviour. As Oh approaches zero, our one-fluid approximation made in the solver Basilisk (Popinet & Collaborators 2013–2024) imposes a no-slip condition at the liquid–gas interface. Resolving this boundary layer requires a minimum grid size of $\Delta \sim KLOh^2$, where L is the characteristic length and K a system-dependent prefactor. This establishes a critical Oh above which results converge well. We empirically determined this as $Oh = 1.17 \times 10^{-4}$ through grid independence testing. Results below this critical value remain unresolved due to insufficient grid resolution, indicated by the pink shaded region in figure 21(*b*). Further computational method improvements are needed to resolve cases where $Oh < 1.17 \times 10^{-4}$.

Appendix D

Figure 25 depicts the qualitative difference in behaviour starting from a cavity with $\varepsilon = 0.091$ (figure 25*a*). Here no jet is seen initially and the wavetrain focusses at $r = 0$ after some time. In figure 25(*b*) with $\varepsilon = 0.242$, a jet is seen at a much earlier time, and no focussing wavetrain is apparent. In this study, we focus on the regime indicated in figure 25(*a*). The jet in figure 25(*b*) is close to the one that was reported in Basak *et al.* (2021), albeit from a single Bessel function.

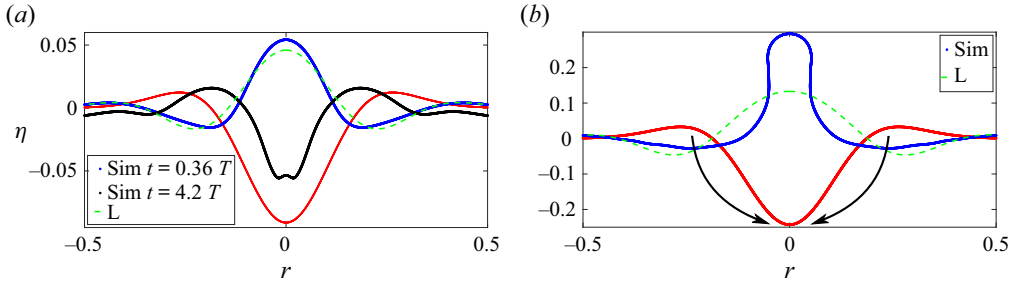

Figure 25. Both (*a*) and (*b*) start with the interface deformed as a cavity shown in red with different ϵ. Here (*a*) (red) interface at $t = 0$, (green dashed curve) numerical simulation and (blue) linear approximation at $t = 0.36T$, when the interface reaches its maximum height and (black curve) at a much later time $t = 4.2T$. (*b*) The same colour code as in (*a*), (blue) for $t = 0.48T$. Here T is the dominant mode time period in the initial spectrum (linear approximation). The arrows in (*b*) indicate the approximate direction of flow resulting from the initial (capillary) pressure gradient. The jet which was studied in Basak *et al.* (2021) from $\eta(r, t = 0) = \varepsilon J_0(k_5 r)$ is closely related to the jet in (*b*). Note the lack of any visible wavetrain when this jet is produced. In this case, pressure difference arising due to the initial steep interface distortion around $r = 0$, triggers a radially inward flow towards the same (indicated with arrows in figure 1*b*). The radial component of this inflow produces a stagnation zone of high pressure at the base of the cavity and a resultant upward jet. We label this situation as 'flow focussing'. This jet in Basak *et al.* (2021) is associated with a large stagnation pressure at its base, involving conversion of kinetic energy (nonlinear term in Bernoulli equation) to pressure energy. In contrast in (*a*), no significant stagnation pressure zone develops initially (as the initial cavity is comparatively less steep compared with panel (*b*)). In this case nonlinear effects become manifest much later when the wavetrain focusses on to the symmetry axis, producing rapid interfacial oscillations at $r = 0$. The apparent importance of nonlinearity around $r = 0$ in this case is somewhat akin to linear dispersive focussing of surface waves, where nonlinearity becomes locally important at the focal point. Here (*a*) $\varepsilon = 0.091$, wave focussing; (*b*) $\varepsilon = 0.242$, flow focussing.

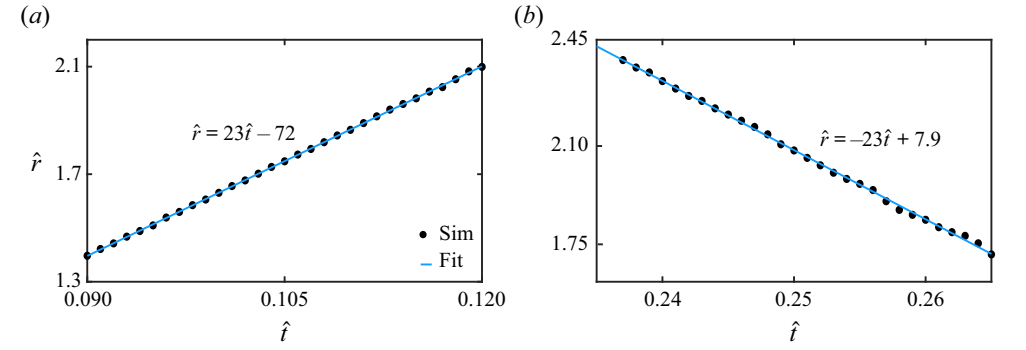

Figure 26. Measurement of interface elevation from simulations for the largest crest following it, for (*a*) outward wave propagation and (*b*) inward propagation. The crests are generated from an initial cavity with $\varepsilon \approx 0.091$ (Case 2 in table 1). The slope of the linear fit indicates the propagation velocity which is approximately equal to the phase speed of the dominant Bessel function. Similar to figure 4(*b*) in Gordillo & Rodríguez-Rodríguez (2019), we observe a good agreement with the linear propagation speed, before and after the reflection.

Appendix E. Comparison with Gordillo & Rodríguez-Rodríguez (2019)

Although the wavetrain in case of bubble bursting ($Bo \ll 1$) (Gordillo & Rodríguez-Rodríguez 2019) is different from the one we study here, some qualitative comparisons can be obtained between the two. In this section, we estimate the speed of propagation of the dominant crest for $\varepsilon = 0.091$ and $Oh = 0$. Similar to the figure 4(*b*) in Gordillo

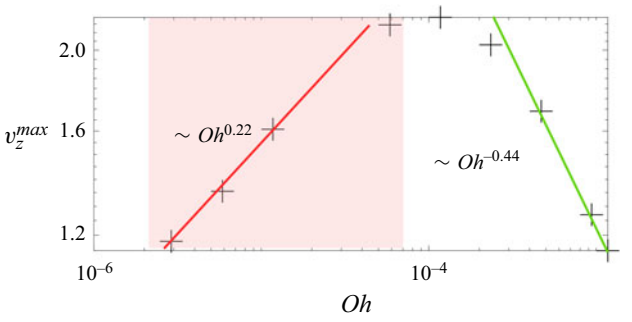

Figure 27. The maximum vertical velocity at the symmetry axis v_z^{max} for different Oh. This figure is a superset of simulation data provided in figure 21(*b*) with additional data points and power-law fits. The data for $Oh < 1.17 \times 10^{-4}$ is indicated as a hashed region to indicate the grid-sensitivity of this data as discussed earlier in Appendix C.

& Rodríguez-Rodríguez (2019), we observe that the waves propagating outwards and inwards propagate with the linear speed. This is validated in figure 26 by tracking the local maxima on the free surface in simulations, before and after reflection. In both cases, the propagation speed agrees with the phase speed of the dominant Bessel function (k_4), see figure 5(*b*). Figure 27 provides an approximate scaling relation (to act as guides only) for the dependence of v_z on Oh. We stress that we do not have theoretical description of these power laws and they are distinct from the $v_z^{max} \sim V_\gamma Oh$ established for bursting bubbles for $Oh > Oh_c$. Unlike the case of bubble bursting seen in figure 12 in the seminal study by Duchemin *et al.* (2002), the intensification seen in v_z^{max} for our case for the optimal Oh_c compared with $Oh \to 0$ is only approximately a factor of two. In the case of bubble bursting, this factor can be as high as 10 (Gordillo & Blanco-Rodríguez 2023). Note that Oh_c appears as a fitting parameter in all existing bursting bubble theories and further work is needed to estimate this value. Our analysis shows that a first-principles theory for this may have to include nonlinearity and also resolve the boundary layer at the interface.

References

Basak, S., Farsoiya, P.K. & Dasgupta, R. 2021 Jetting in finite-amplitude, free, capillary-gravity waves. *J. Fluid Mech.* **909**, A3.

Benjamin, T.B. & Feir, J.E. 1967 The disintegration of wave trains on deep water. Part 1. Theory. *J. Fluid Mech.* **27** (3), 417–430.

Brown, M.G. & Jensen, A. 2001 Experiments on focusing unidirectional water waves. *J. Geophys. Res.: Oceans* **106** (C8), 16917–16928.

Charlie Wood 2020 The grand unified theory of rogue waves. https://www.quantamagazine.org/the-grand-unified-theory-of-rogue-waves-20200205.

Chavarria, G.R., Le Gal, P. & Le Bars, M. 2018 Geometrical focusing of surface waves. *Phys. Rev. Fluids* **3** (9), 094803.

Davis, M.C. & Zarnick, E.E. 1964 Testing ship models in transient waves. In *5th Symposium on Naval Hydrodynamics*, vol. 507. DTIC.

Deike, L. 2022 Mass transfer at the ocean–atmosphere interface: the role of wave breaking, droplets, and bubbles. *Annu. Rev. Fluid Mech.* **54**, 191–224.

Deike, L., Ghabache, E., Liger-Belair, G., Das, A.K., Zaleski, S., Popinet, S. & Séon, T. 2018 Dynamics of jets produced by bursting bubbles. *Phys. Rev. Fluids* **3** (1), 013603.

Dhote, Y., Kumar, A., Kayal, L., Goswami, P.S. & Dasgupta, R. 2024 Standing waves and jets on a sessile, incompressible bubble. *Phys. Fluids* **36** (1), 012105.

Dubrulle, B. 2019 Beyond Kolmogorov cascades. *J. Fluid Mech.* **867**, P1.

Duchemin, L., Popinet, S., Josserand, C. & Zaleski, S. 2002 Jet formation in bubbles bursting at a free surface. *Phys. Fluids* **14** (9), 3000–3008.

DUREY, M. & MILEWSKI, P.A. 2023 Resonant triad interactions of gravity waves in cylindrical basins. *J. Fluid Mech.* **966**, A25.
DYSTHE, K., KROGSTAD, H.E. & MÜLLER, P. 2008 Oceanic rogue waves. *Annu. Rev. Fluid Mech.* **40**, 287–310.
EGGERS, J. 2018 Role of singularities in hydrodynamics. *Phys. Rev. Fluids* **3** (11), 110503.
EGGERS, J.G., SPRITTLES, J. & SNOEIJER, J.H. 2024 Coalescence dynamics. *Annu. Rev. Fluid Mech.* **57**.
FARSOIYA, P.K., MAYYA, Y.S. & DASGUPTA, R. 2017 Axisymmetric viscous interfacial oscillations – theory and simulations. *J. Fluid Mech.* **826**, 797–818.
FILLETTE, J., FAUVE, S. & FALCON, E. 2022 Axisymmetric gravity-capillary standing waves on the surface of a fluid. *Phys. Rev. Fluids* **7** (12), 124801.
GHABACHE, E., ANTKOWIAK, A., JOSSERAND, C. & SÉON, T. 2014*a* On the physics of fizziness: how bubble bursting controls droplets ejection. *Phys. Fluids* **26** (12), 121701.
GHABACHE, É., SÉON, T. & ANTKOWIAK, A. 2014*b* Liquid jet eruption from hollow relaxation. *J. Fluid Mech.* **761**, 206–219.
GORDILLO, J.M. & BLANCO-RODRÍGUEZ, F.J. 2023 Theory of the jets ejected after the inertial collapse of cavities with applications to bubble bursting jets. *Phys. Rev. Fluids* **8** (7), 073606.
GORDILLO, J.M. & RODRÍGUEZ-RODRÍGUEZ, J. 2019 Capillary waves control the ejection of bubble bursting jets. *J. Fluid Mech.* **867**, 556–571.
HASSELMANN, K. 1962 On the non-linear energy transfer in a gravity-wave spectrum. Part 1. General theory. *J. Fluid Mech.* **12** (4), 481–500.
HENRI COHEN, F.R.V. & ZAGIER, D. 2000 Convergence acceleration of alternating series. *Expl Maths* **9** (1), 3–12.
JOHANNESSEN, T.B. & SWAN, C. 2001 A laboratory study of the focusing of transient and directionally spread surface water waves. *Proc. R. Soc. Lond.* A **457** (2008), 971–1006.
JOSEPH, D.D. 2006 Potential flow of viscous fluids: historical notes. *Intl J. Multiphase Flow* **32** (3), 285–310.
KAYAL, L. 2024 Codes for cavity evolution. https://github.com/Lohittitas/concentricWave.
KAYAL, L., BASAK, S. & DASGUPTA, R. 2022 Dimples, jets and self-similarity in nonlinear capillary waves. *J. Fluid Mech.* **951**, A26.
KAYAL, L. & DASGUPTA, R. 2023 Jet from a very large, axisymmetric, surface-gravity wave. *J. Fluid Mech.* **975**, A22.
KIENTZLER, C.F., ARONS, A.B., BLANCHARD, D.C. & WOODCOCK, A.H. 1954 Photographic investigation of the projection of droplets by bubbles bursting at a water surface. *Tellus* **6** (1), 1–7.
LOHSE, D. & SHISHKINA, O. 2024 Ultimate Rayleigh–Bénard turbulence. *Rev. Mod. Phys.* **96** (3), 035001.
LONGUET-HIGGINS, M.S. 1974 Breaking waves in deep or shallow water. In *Proc. 10th Conf. on Naval Hydrodynamics*, vol. 597, p. 605. MIT.
LONGUET-HIGGINS, M.S. 1983 Bubbles, breaking waves and hyperbolic jets at a free surface. *J. Fluid Mech.* **127**, 103–121.
LONGUET-HIGGINS, M.S. 1990 An analytic model of sound production by raindrops. *J. Fluid Mech.* **214**, 395–410.
MACINTYRE, F. 1968 Bubbles, boundary-layer 'microtome' for micronthick samples of a liquid surface. *J. Phys. Chem.* **72** (2), 589–592.
MACINTYRE, F. 1972 Flow patterns in breaking bubbles. *J. Geophys. Res.* **77** (27), 5211–5228.
MACK, L.R. 1962 Periodic, finite-amplitude, axisymmetric gravity waves. *J. Geophys. Res.* **67** (2), 829–843.
MALLORY, J.K. 1974 Abnormal waves on the south east coast of South Africa. *Intl Hydrograph. Rev.* **LI** (2).
MCALLISTER, M.L., DRAYCOTT, S., DAVEY, T., YANG, Y., ADCOCK, T.A.A., LIAO, S. & VAN DEN BREMER, T.S. 2022 Wave breaking and jet formation on axisymmetric surface gravity waves. *J. Fluid Mech.* **935**, A5.
MCIVER, M. 1985 Diffraction of water waves by a moored, horizontal, flat plate. *J. Engng Maths* **19** (4), 297–319.
MEI, C.C. & LIU, L.F. 1973 The damping of surface gravity waves in a bounded liquid. *J. Fluid Mech.* **59** (2), 239–256.
MILES, J.W. 1968 The cauchy–poisson problem for a viscous liquid. *J. Fluid Mech.* **34** (2), 359–370.
MILES, J.W. 1976 Nonlinear surface waves in closed basins. *J. Fluid Mech.* **75** (3), 419–448.
MOORE, D.W. 1963 The boundary layer on a spherical gas bubble. *J. Fluid Mech.* **16** (2), 161–176.
MPMATH 2023 *mpmath: a Python library for arbitrary-precision floating-point arithmetic (version 1.3.0)*. http://mpmath.org/.
MURASHIGE, S. & KINOSHITA, T. 1992 An ideal ocean wave focusing lens and its shape. *Appl. Ocean Res.* **14** (5), 275–290.
NAYFEH, A.H. 1987 Surface waves in closed basins under parametric and internal resonances. *Phys. Fluids* **30** (10), 2976–2983.

OGUZ, H.N. & PROSPERETTI, A. 1990 Bubble entrainment by the impact of drops on liquid surfaces. *J. Fluid Mech.* **219**, 143–179.

ONORATO, M., RESIDORI, S., BORTOLOZZO, U., MONTINA, A. & ARECCHI, F.T. 2013 Rogue waves and their generating mechanisms in different physical contexts. *Phys. Rep.* **528** (2), 47–89.

ONSAGER, L. 1949 Statistical hydrodynamics. *Il Nuovo Cimento* **6** (2), 279–287.

PENNEY, W.G., PRICE, A.T., MARTIN, J.C., MOYCE, W.J., PENNEY, W.G., PRICE, A.T. & THORNHILL, C.K. 1952 Part II. Finite periodic stationary gravity waves in a perfect liquid. *Phil. Trans. R. Soc. Lond.* A **244** (882), 254–284.

PEREGRINE, D.H. 1976 Interaction of water waves and currents. *Adv. Appl. Mech.* **16**, 9–117.

PEREGRINE, D.H. 1986 Approximate descriptions of the focussing of water waves. In *Coastal Engineering 1986*, pp. 675–685. ASCE.

POPINET, S. & COLLABORATORS 2013–2024 Basilisk C: volume of fluid method. http://basilisk.fr.

PRANDTL, L. 1904 Über flüssigkeitsbewegung bei sehr kleiner reibung. *Math-Kongr, Heidelberg*, 484–491.

PROSPERETTI, A. 1976 Viscous effects on small-amplitude surface waves. *Phys. Fluids* **19** (2), 195–203.

PROSPERETTI, A. 1981 On the motion of two superposed viscous fluids. *Phys. Fluids* **24**, 1217–1223.

RACKAUCKAS, C. & NIE, Q. 2019 Confederated modular differential equation APIs for accelerated algorithm development and benchmarking. *Adv. Engng Softw.* **132**, 1–6.

RACKAUCKAS, C., NIE, Q. & COLLABORATORS 2017 Differentialequations.jl – a performant and feature-rich ecosystem for solving differential equations in julia. *J. Open Res. Softw.* **5** (1), 15.

RAPP, R.J. & MELVILLE, W.K. 1990 Laboratory measurements of deep-water breaking waves. *Phil. Trans. R. Soc. Lond.* A **331** (1622), 735–800.

SANJAY, V. 2022 Viscous free-surface flows. PhD thesis, University of Twente.

SANJAY, V., CHANTELOT, P. & LOHSE, D. 2023 When does an impacting drop stop bouncing? *J. Fluid Mech.* **958**, A26.

SANJAY, V. & LOHSE, D. 2024 Unifying theory of scaling in drop impact: Forces & maximum spreading diameter. arXiv:2408.12714.

SANJAY, V., LOHSE, D. & JALAAL, M. 2021 Bursting bubble in a viscoplastic medium. *J. Fluid Mech.* **922**, A2.

SANJAY, V., SEN, U., KANT, P. & LOHSE, D. 2022 Taylor–Culick retractions and the influence of the surroundings. *J. Fluid Mech.* **948**, A14.

SMITH, R. 1976 Giant waves. *J. Fluid Mech.* **77** (3), 417–431.

SNOEIJER, J.H. & ANDREOTTI, B. 2013 Moving contact lines: scales, regimes, and dynamical transitions. *Annu. Rev. Fluid Mech.* **45** (1), 269–292.

STAMNES, J.J., LØVHAUGEN, O., SPJELKAVIK, B., MEI, C.C., LO, E. & YUE, D.K.P. 1983 Nonlinear focusing of surface waves by a lens–theory and experiment. *J. Fluid Mech.* **135**, 71–94.

STRUTT, J.W. 1915 Deep water waves, progressive or stationary, to the third order of approximation. *Proc. R. Soc. Lond.* A **91** (629), 345–353.

STUHLMAN, O. JR. 1932 The mechanics of effervescence. *Physics* **2** (6), 457–466.

THE EDITORS OF ENCYCLOPAEDIA BRITANNICA 2024 Aghulas current. https://www.britannica.com/place/Agulhas-Current.

TORRES, T., LLOYD, M., DOLAN, S.R. & WEINFURTNER, S. 2022 Wave focusing by submerged islands and gravitational analogues. *Phys. Rev. Res.* **4** (3), 033210.

TSAI, W.-T. & YUE, D.K.P. 1987 Numerical calculation of nonlinear axisymmetric standing waves in a circular basin. *Phys. Fluids* **30** (11), 3441–3447.

VILLERMAUX, E., WANG, X. & DEIKE, L. 2022 Bubbles spray aerosols: certitudes and mysteries. *PNAS Nexus* **1** (5), pgac261.

WHITE, B.S. & FORNBERG, B. 1998 On the chance of freak waves at sea. *J. Fluid Mech.* **355**, 113–138.

WILDEMAN, S., VISSER, C.W., SUN, C. & LOHSE, D. 2016 On the spreading of impacting drops. *J. Fluid Mech.* **805**, 636–655.

WU, C.H. & NEPF, H.M. 2002 Breaking criteria and energy losses for three-dimensional wave breaking. *J. Geophys. Res.: Oceans* **107** (C10), 41.

XU, C. & PERLIN, M. 2023 Parasitic waves and micro-breaking on highly nonlinear gravity–capillary waves in a convergent channel. *J. Fluid Mech.* **962**, A46.

ZAKHAROV, V.E., DYACHENKO, A.I. & PROKOFIEV, A.O. 2006 Freak waves as nonlinear stage of stokes wave modulation instability. *Eur. J. Mech. (B/Fluids)* **25** (5), 677–692.

ZHANG, F.H. & THORODDSEN, S.T. 2008 Satellite generation during bubble coalescence. *Phys. Fluids* **20** (2), 022104.